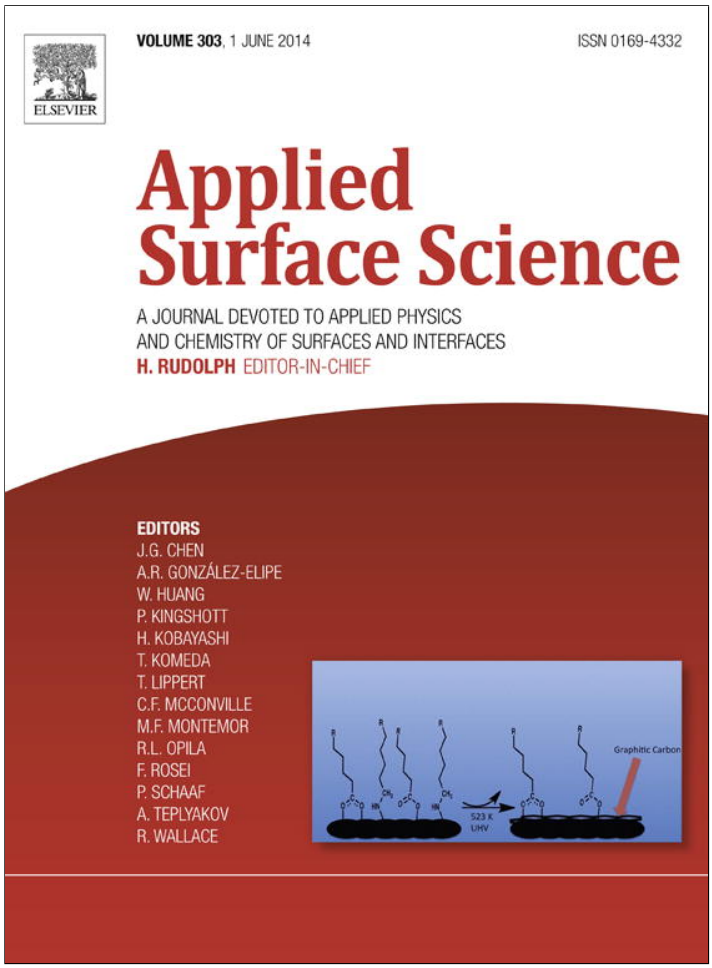

Applied Surface Science 303 (2014) 217–232

Contents lists available at ScienceDirect

Applied Surface Science

journal homepage: www.elsevier.com/locate/apsusc

Effect of oblique incidence on silver nanomaterials fabricated in water via ultrafast laser ablation for photonics and explosives detection

G. Krishna Podagatlapalli[a], Syed Hamad[b], Md. Ahamad Mohiddon[c], S. Venugopal Rao[a,*]

[a] Advanced Center of Research in High Energy Materials (ACRHEM), University of Hyderabad, Prof. C. R. Rao Road, Hyderabad 500046, India
[b] School of Physics, University of Hyderabad, Prof. C. R. Rao Road, Hyderabad 500046, India
[c] Centre for Nanotechnology University of Hyderabad, Prof. C. R. Rao Road, Hyderabad 500046, India

ARTICLE INFO

Article history:
Received 5 November 2013
Received in revised form 24 February 2014
Accepted 25 February 2014
Available online 12 March 2014

PACS:
79.20.Eb
78.30.−j
42.65.Re
42.65.−k

Keywords:
Ultrafast ablation
Silver nanoparticles
Silver nanostructures
Explosives
SERS
Degenerate four wave mixing

ABSTRACT

Picosecond (ps) laser ablation of silver (Ag) substrate submerged in double distilled water was performed at 800 nm for different angles of incidence of 5°, 15°, 30° and 45°. Prepared colloidal solutions were characterized through transmission electron microscopy, UV absorption spectroscopy to explore their morphologies and surface plasmon resonance (SPR) properties. Third order nonlinear optical (NLO) characterization of colloids was performed using degenerate four wave mixing (DFWM) technique with ~40 fs laser pulses at 800 nm and the NLO coefficients were obtained. Detailed analysis of the data obtained from colloidal solutions suggested that superior results in terms of yield, sizes of the NPs, SPR peak position were achieved for ablation performed at 30° incident angle. Surface enhanced Raman spectra (SERS) of Rhodamine 6G from nanostructured substrates were investigated using excitation wavelengths of 532 and 785 nm. In both the cases substrates prepared at 30° incident angle exhibited superior enhancement in the Raman signatures with a best enhancement factor achieved being $>10^8$. SERS of an explosive molecule 5-amino, 3-nitro, -1H-1,2,4-nitrozole (ANTA) was also demonstrated from these nanostructured substrates. Multiple usage of Ag nanostructures for SERS studies revealed that structures prepared at 30° incident angle provided superior performance amongst all.

1. Introduction

Versatility and extreme simplicity are significant features of top-down process of pulsed laser ablation of bulk silver targets submerged in liquids (PLAL) [1–15]. The technique facilitates fabrication of impurity free Ag nanoparticles (NPs) and well textured Ag metallic nanostructures (NSs) in a short time without contamination of the environment since rupture of the metal target takes place underneath the liquid layer. Simultaneous fabrication of the NPs and NSs in a single step is not possible with most of the other established lithographic methods. Moreover, products of PLAL (NSs and NPs) need not be treated using separate chemicals since the method itself is green and free from precursors or surfactants akin to other techniques [16,17]. Aforesaid salient features of PLAL technique renders it to play a crucial role in plasmonics, photonics, and biosciences. Wide range applications of plasmonic (Ag) NPs include anti-bacterial [18,19] agents, cancer cell destroyers [20,21], elements in device making of optical limiters and essential building blocks of solar cell fabrication etc. [22,23]. Similarly, Ag nanostructured surfaces play a decisive role in surface enhanced Raman scattering spectroscopy (SERS) [24–30] for trace detection of adsorbed molecules, including potential explosives [31].

In PLAL, a focused pulsed laser beam is allowed to fall on a metallic target submerged in liquid, leading to absorption of the laser pulse energy through the conduction electrons of metal target via inverse Bremsstrahlung. Consequently, ejected ballistic electron gas attains higher temperatures than the surrounding lattice which remain cold. After a few ps [32,33] electron gas at higher temperature transfers heat energy to lattice through electron-phonon coupling achieving a state of equilibrium. Gradient of temperatures of ballistic electron gas, lattice system and the dynamics of equilibrium are successfully explained by a two-temperature model [34]. Post equilibration, if the temperature attained by entire system is greater than melting point of metal target then portion of metal at which laser energy is deposited turns to melt phase. The metallic melt acts as a reservoir for fabrication of NPs and NSs. A complicated laser-matter interaction under the liquid layer leads to the

* Corresponding author. Tel.: +91 040 23138811.
E-mail addresses: svrsp@uohyd.ernet.in, soma_venu@yahoo.com, soma_venu@uohyd.ac.in (S. Venugopal Rao).

http://dx.doi.org/10.1016/j.apsusc.2014.02.152
0169-4332/

generation of plasma plume at the point where the local melting has taken place. Later, the plasma expands into surrounding liquid medium resulting in generation of a shockwave. During the process of expansion, plasma plume cools down and transfers the energy to liquid medium. Consequently, cavitation bubble [35] is generated in the liquid medium which further expands. After a certain period (typically a few hundred microseconds) where inside pressure decreases compared to the surrounding liquid medium, cavitation bubble collapses followed by generation of a second shock wave [36]. In fact, the exact stage at which nanomaterials are fabricated is still being debated. Some groups, through extensive experimental research and modeling, have suggested that the nanomaterials are generated during the expansion of cavitation bubble inside it on a time scale of the order 10^{-6}–10^{-4} s [37,38]. The expansion of cavitation bubble into liquid medium exerts a recoil pressure on the metallic melt formed under plasma plume. Recoil pressure splashes the melt and residual recoil pressure redistributes the metallic melt. Former process guides the fabrication of nanoparticles and latter leads to the fabrication of nanostructures. Nanoentities inside the cavitation bubble are at a higher temperature than liquid environment. Ag nano-materials exhibit fascinating electronic, optical, and other physical properties depending on their crystallinity, composition, shape, and size. Furthermore, Ag NPs support strong localization of surface plasmon resonances (LSPR) [39–41] than the other well known plasmonic metals. Besides, Ag colloids and nanostructured Ag targets (with grating formation along with the presence of Ag nanoparticle grains) act as an efficient SERS active platform through the excitation of propagating surface plasmons (surface plasmon polaritons) and non-propagating surface plasmons (localized surface plasmons) [42,43].

Size and shape of the fabricated metallic nanomaterials in PLAL not only depend on laser parameters [44–48] such as wavelength, pulse duration, energy per pulse, repetition rate, beam waist at the focus, number of laser pulses per spot but also on the nature of surrounding liquid. Extensive studies of laser ablation in liquids investigating some of these parameters and resulting applications of the generated NPs have been performed by Meunier group [49–53]. Amendola et al. [36] carried out an extensive study of PLAL through formation of cavitation bubble and provided a panoramic view of how the various laser parameters and the nature of liquid influenced ablation in a qualitative manner. However, very few articles extensively dealt with detailed dynamics of laser ablation in liquid and dependence of products on laser parameters [54–56]. Notwithstanding several works reporting fabrication of Ag nanomaterials (both NPs and NSs) through pulsed laser ablation in liquids, effect of nonzero angle of incidence has not yet been attempted/reported. Earlier reports have demonstrated the effect of lateral beam waist on ablation but not the axial beam waist which is also the part of ablation when the angle of incidence is changed. Ganeev and Jia [57] investigated surface modifications of silicon through laser ablation with fs pulses at an angle of incidence close to Brewster angle using interferometry and studied the dependence of grating period on the angle of incidence. Sing and Tripathi [58] dealt the laser beat wave excitation of surface plasma wave at an oblique incidence of laser beams through which beams exerted a ponder motive force on free electrons at the frequency of beat, consequently producing a nonlinear current that drives plasma wave resonantly. The surface plasma wave causes an efficient heating of electron system which leads to ablation of material and thus the dependence of ablation on angle of incident laser beam was retrieved theoretically. George et al. [59] reported the angular dependence of focused ns laser pulses on to polymer films at moderate energies revealing the control of complex nanostructure formation at oblique incidences.

In our earlier works, fabrication and effects of polarity of liquid medium was investigated through ablation studies of Al targets in polar and non-polar liquid media [15]. The effects of over writing (multiple/double/single line ablation) of Ag/Cu substrates in different liquid media were also investigated along with the Raman activity of fabricated NSs/NPs [46,60]. In continuation of our earlier work, dependence of non-zero angle of incidence on ablation of Ag substrate in double distilled water is investigated in the present work. Most of the earlier studies of ablation at non-zero angle of laser incidence were carried out in ambient air and that too for non-metals. In the present work we attempted to (a) fabricate the Ag nanomaterials for 5°, 15°, 30°and 45° angle of laser incidence on the target surface (experiments were also repeated for constant fluence on the target surface at these four angles of incidence) (b) investigate the specific angle of incidence at which superior products were achieved after ablation (c) characterize the nonlinear optical (NLO) properties of the prepared Ag colloids using fs degenerate four wave mixing (fs-DFWM) at 800 nm in the BOXCARS geometry (d) investigate surface enhanced Raman activity of Ag substrates fabricated at different angles of incidence with Rhodamine 6G (μM concentration) in methanol excited with 532 nm and 785 nm (d) record the Raman spectra of high explosive molecule of 5-amino-3-nitro-1H-1,2,4-triazole (ANTA) at mM and μM concentrations. In this communication we also report the multiple utility of Ag NSs when combined with appropriate cleaning methods.

2. Experimental details

Complete details of the experimental setup are presented in our earlier works [15,46]. Briefly, Ag substrate submerged in double distilled water in a Pyrex cell and was positioned on a motorized *X*–*Y* stage. In our earlier fabrication experiments (of Ag NPs) achieved through double line ablation, thickness of liquid layer used was ~2–3 mm whereas in the present case liquid level was maintained at ~5 mm so as to accommodate the angle dependent ablation. Initially plane polarized (P-polarization) laser pulses were allowed to focus vertically onto the Ag substrate through a plano-convex lens of focal length 25 cm. Optimization near focus was carried out by observing intense plasma plume and cracking sound when focused laser beam impinged on the metallic target [61,62]. Angle of incidence was altered by tilting the mirror which was directing focused laser beam onto target surface. The angle of incidence was adjusted and confirmed by a protractor whose center was placed at the position of visible plasma plume. The schematic of non-zero angle of laser incidence carried out on Ag substrate is illustrated in Fig. 1(a). *X*–*Y* translation stages, interfaced to Newport ESP 300 motion controller, were utilized to draw periodic line structures on the Ag substrate with separations of ~20 μm. Fig. 1(b) illustrates the schematic of single line and multiple line ablation mechanisms. The scanning speeds of the *X*–*Y* stages were ~0.1 and ~0.4 mm/s. The uncertainty in adjusting focus exactly on the metal substrate because of displacement caused by refractive index of surrounding liquid and other nonlinear optical effects was taken care of by observing the plasma [63]. The theoretical lateral beam waist ($\omega_{lateral}$) estimated at focus (in air) was ~10 μm while the theoretical axial beam waist (ω_{axial}) was ~20 μm. However, in reality beam waist at focus on the target surface immersed in water will not be the same as in air. Estimated beam waist at focus is nearly double that of the waist in air. Barcikowski et al. [64] explained the width of line structure can be approximated to $2\omega_0$ when the ablation is carried out by ultrafast laser pulses. For exact beam waist estimation, craters were made on Ag target immersed in double distilled water (5 mm above target surface) to estimate the degree of stretch and depth. Accordingly, axial beam waist (ω_0) in the present experiment was estimated to be ~40 μm, based on the diameters of craters created with 90,000 pulses (exposure time of 90 s at normal incidence). For each tilting angle effective liquid layer thickness was

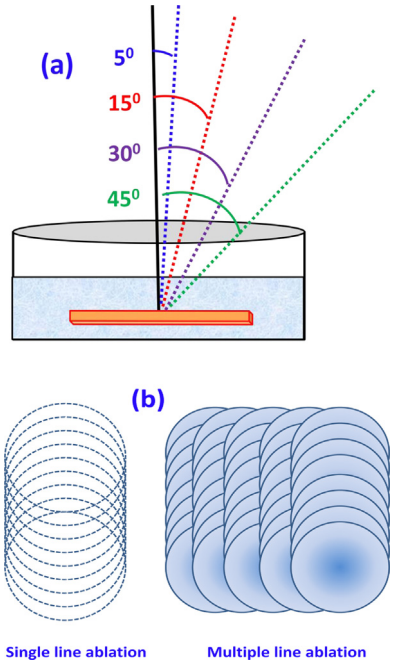

Fig. 1. (a) Experimental scheme of laser ablation of Ag substrate immersed in double distilled water with different angles of laser incidence with respect to the normal (b) Schematic of single line and multiple line ablation.

measured [63,65] from the cosine angle. From the effective thickness of liquid layer dz_l (the extent to which focusing lens has to be displaced) was measured. This estimate revealed that the positions of lens to be displaced [to adjust the focus to be exactly on target surface], were ~1.25, ~1.3, ~1.4 and ~1.7 mm for angles of incidence of 5°, 15°, 30° and 45°, respectively. After the adjustment of focus craters are created at each incident angle to quantify the laser fluence on target surface by allowing 90,000 pulses on to the surface. FESEM images of thus crated craters are depicted in Fig. 2.

Input pulse energy used for four angles was kept constant (i.e. 200 μJ) so as to ensure constant fluence on the target surface for each case. However, from the images of the craters effective fluences on the target surface for the incident angles 5°, 15°, 30° and 45° were estimated to be ~4.2, ~3.2, ~2.4 and ~2.2 J/cm^2, respectively. Form factors were also estimated for all the four cases as ~1, ~0.99, ~0.98 and ~0.97. After completion of the ablation, Ag substrates were removed and preserved after nominal cleaning procedures. Colloidal suspensions were preserved in air tightened glass vials. To avoid ambiguity the Ag colloids in distilled water prepared at 5°, 15°, 30° and 45° angle of laser incidence on the target surface are designated as NP-5, NP-15, NP-30 and NP-45 where as substrates are labeled as NS-5, NS-15, NS-30 and NS-45.

UV–vis spectrometer (Jasco-V-670) was utilized to record the absorption spectra of NP-5, NP-15, NP-30 and NP-45 in the spectral range of 250 nm-800 nm. Ag suspensions were characterized by TEM (FEI Tecnai G2 S-Twin 200 kV instrument) to estimate size distribution, morphologies and crystallinity of the NPs. Surface morphology of NS-5, NS-15, NS-30 and NS-45 were characterized by FESEM (Ultra 55 from Carl ZEISS) and an AFM (Seiko instruments). NLO properties of NPs colloidal solutions were investigated using fs-DFWM [66–70] in the BOXCAR geometry [with 1 kHz, 800 nm laser pulses (~2 mJ, ~40 fs duration)]. Experimental schematic of fs-DFWM is shown in Fig. 3. The ultrafast NLO properties of Ag suspensions depend on factors such as yield, size and morphologies of the NPs. Spatial overlap of the three fundamental laser pulses was achieved using a lens of focal length of 15 cm

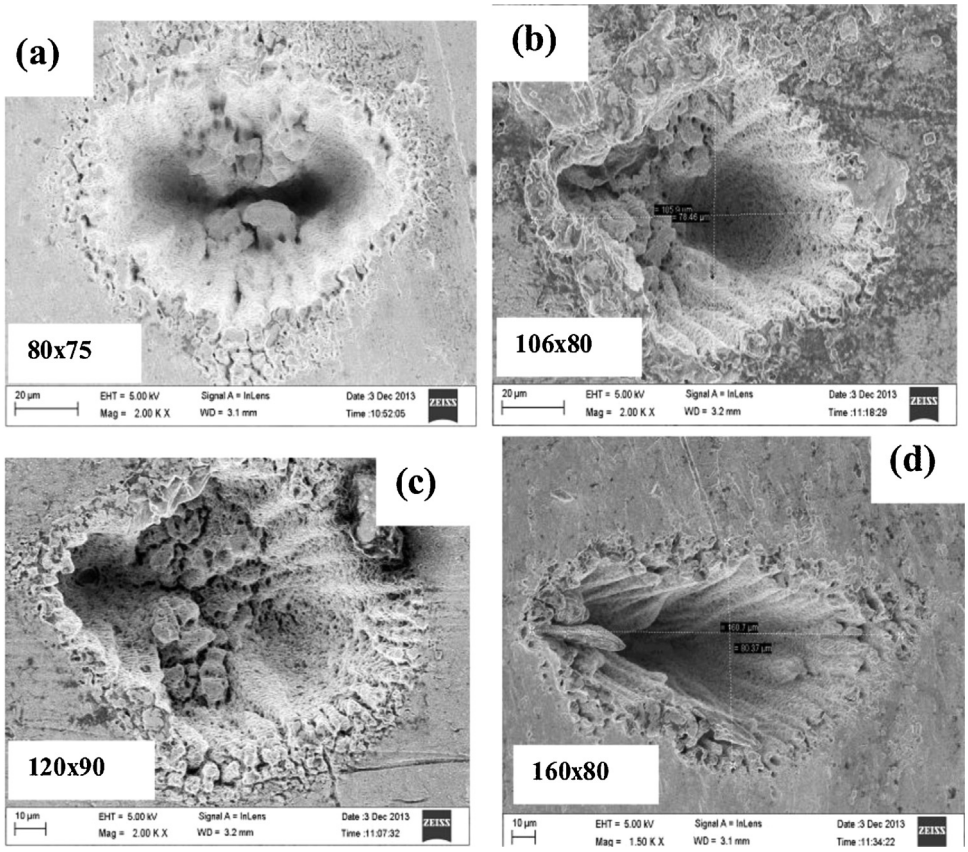

Fig. 2. FESEM images of the craters created at (a) 5°, (b) 15°, (c) 30°, and (d) 45° angles of incidence. Laser beam was focused on the target for 90 s.

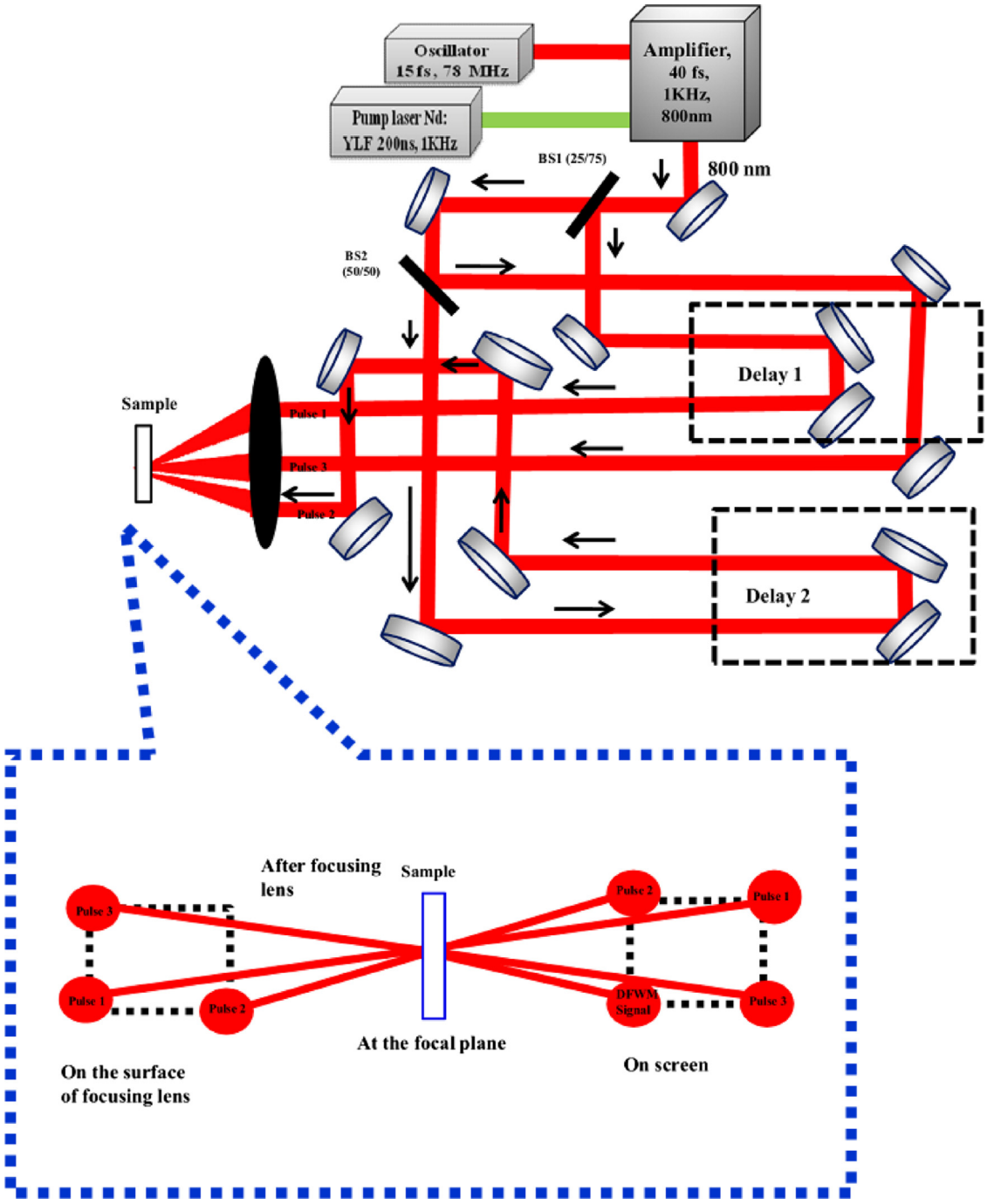

Fig. 3. Experimental schematic of femtosecond degenerate four wave mixing in the BOXCARS geometry.

at the sample (Ag suspensions) placed in a cuvette (5 mm path length) made of quartz. Lens with longer focal length was utilized to increase the volume of interaction in the sample. Motorized stage (Newport-MILS 100 MTVP) with a resolution of 0.5 μm, interfaced to ESP motion controller through a Lab VIEW program, was used to accomplish temporal overlap of the three fundamental pulses of ~40 fs duration. The four wave mixing transients were recorded as a function of probe (pulse 2 in Fig. 2) delay in steps of 0.066 ps with a fast photodiode (SM1PD2A) which was connected to lock-in amplifier (Signal Recovery 7265). Typical input energies used were ~50 μJ.

Raman spectra of R6G/ANTA [structures of molecules are shown in Fig. 1 of supporting information (SI)] adsorbed on NS-5, NS-15, NS-30 and NS-45 were recorded with micro-Raman (WiTec ALPHA 300 instrument) and bulk Raman spectrometers (Ocean Optics), which used continuous wave (cw) Nd:YAG laser at 532 nm and a cw Ar^+ laser at 785 nm, respectively. Raman spectra of R6G (10 μL) was recorded from the structured Ag substrates. Acquisition time for recording was 5 s and all spectra and was calibrated with Raman peak of silicon wafer at 520 cm^{-1}. In the Micro Raman spectrometer laser beam was focused on the substrate using an objective lens (100×) and the theoretical beam waist estimated was ~700 nm. In bulk Raman spectrometer (excitation at 785 nm), laser beam (diameter of ~1 mm) was directed toward sample without any focusing lenses and Raman signals were collected in back scattering geometry.

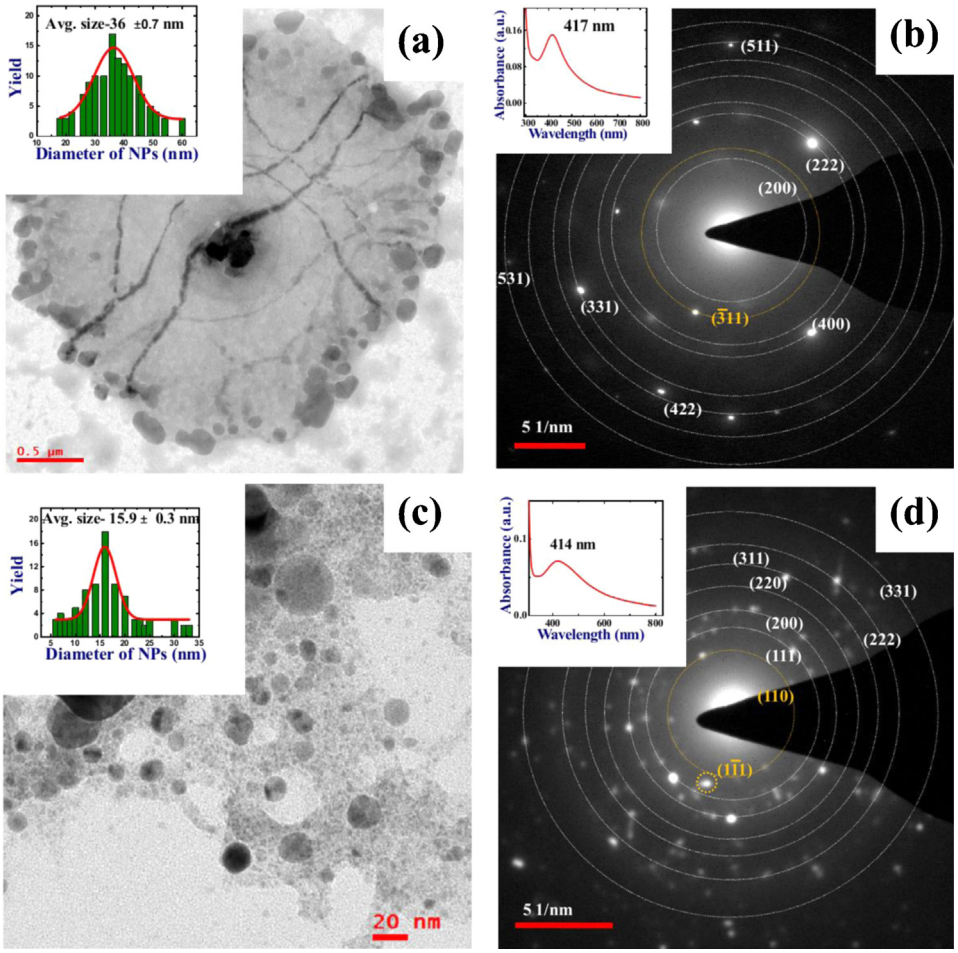

Fig. 4. (a) TEM image of NP-5 and inset shows distribution histogram illustrating an average size of ~36 nm (b) SAED pattern of NPs in NP-5 with proper plane assignments and inset depicts UV–vis absorption spectra with SPR peak near 417 nm (c) TEM image of NP-15 and inset shows distribution histogram illustrates an average size of ~16 nm (d) SAED pattern of NPs in NP-15 and inset depicts UV–vis absorption spectra with SPR peak near 414 nm. Yellow color indicates the plane corresponding to oxidized phase. (For interpretation of the references to color in this figure legend, the reader is referred to the web version of the article.)

3. Results and discussion

3.1. Characterizations of Ag colloids

The morphology and average particle size distribution of the Ag colloids NP-5, NP-15, NP-30 and NP-45 along with crystallographic phase investigations were carried out by bright field TEM imaging and SAED techniques. The particle size distributions were drawn from TEM bright field images and were supported by localized surface plasmon resonance (LSPR) peak position of Ag suspensions. Figs. 4(a), (c) and 5(a), (c) represent the bright field TEM images of NP-5, NP-15, NP-30 and NP-45 nanoparticles, respectively. All the images had similar behavior of varying particle dimensions with a central peak size, exhibiting approximate Gaussian like distribution. Gatan digital micrograph software provided with the TEM instrument was utilized to estimate the average size of the NPs. Manual estimation of particle sizes has been carried out and size distribution histogram is depicted in the insets [Figs. 4(a), (c) and 5(a), (c)], respectively. The calculated peak average particle size for NP-5, NP-15, NP-30 and NP-45 were ~36 nm (range of 18–60 nm), ~16 nm (range of 6–33 nm), ~14 nm (range of 5–25 nm), ~20 nm (range of 6–32 nm), respectively. Histogram construction from the frequencies of available NPs information is tabulated in supporting information. In addition to spherical NPs, fine nano-ribbons with the dimensions of few tens of nanometers were observed in Fig. 4(a) of NP-5 bright field image. At present we are unable to completely explain the origin of diverse sized NPs with a range of distribution since it needs a detailed theoretical understanding of cavitation bubble formation and its time dependent behavior. Following their ns ablation studies, Wagener et al. [71] demonstrated that the oscillations of the cavitation bubble causes production of different nanoparticles and agglomerates. We believe the cavitation bubble oscillation dynamics might be different for different angles of laser incidence which resulted in the formation of different sized NPs. Moreover, as the liquid medium comprises oxygen, instantaneous interference of Ag metallic plume with it could have resulted in fabrication of core shell (oxide cladding) type NPs.

The crystallographic information drawn from SAED patterns of NP-5, NP-15, NP-30 and NP-45 are presented in Figs. 4(b), (d) and 5(b), (d), respectively. The SAED pattern has concentric rings along with few bright diffraction spots, which demonstrates the polycrystalline nature of Ag NPs. The typical diffraction aperture used in our SAED study selects a minimum dimension of 200 nm circular area on the sample, under which it is impossible to diffract a single particle in this study. The presented SAED pattern was recorded with certain number of NPs selected over crowded NPs area on the grid. Due to this reason the presented SAED diffraction ring patterns are slightly distorted from symmetric arrangement. These patterns were improved by drawing a dotted line for better visuals. The calculated diameter of concentric ring pattern from inside to outside were 2.3, 2.0, 1.4, 1.2,

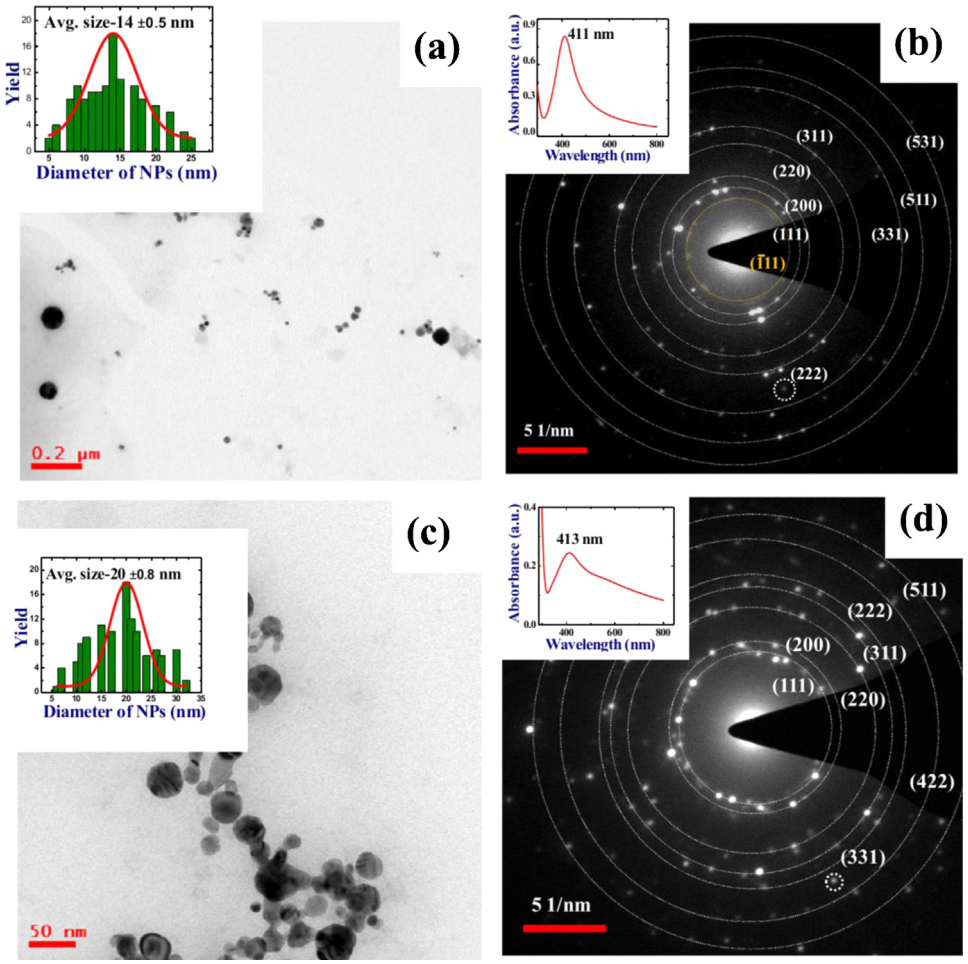

Fig. 5. (a) TEM image of NP-30 and inset shows distribution histogram illustrating an average size of ~14 nm (b) SAED pattern of NPs in NP-30 and inset depicts UV–vis absorption spectra with SPR peak near 411 nm (c) TEM image of NP-45 and inset shows distribution histogram illustrates an average size of ~20 nm (b) SAED pattern of NPs in NP-15 and inset depicts UV–vis absorption spectra with SPR peak near 413 nm. Yellow color indicates the plane corresponding to oxidized phase. (For interpretation of the references to color in this figure legend, the reader is referred to the web version of the article.)

1.1, 0.9, 0.8, 0.7 and 0.6 Å. In general the diameter of ring pattern is assigned to interplanar separation of crystallographic structure from which SAED has been performed. These interplanar distances exactly coincide with FCC (face centered cube) phase of pure Ag as mentioned in PCPDF file No. 01-1167 [72]. The above mentioned distances are indexed in same order as (1 1 1), (2 0 0), (2 2 0), (3 1 1), (2 2 2), (3 3 1), (4 2 2), (5 1 1), (5 3 1) respectively. Along with pure Ag pattern we have observed few additional weak diffraction spots and ring patterns, which are presented by the colored ring in Figs. 4(b), (d) and 5(b). The interplanar distance measured for these additional spots were found to match with monoclinic phase of AgO (PCPDF file No. 84-1547) [73]. The measured distances and their indexing were 3.0 Å (1 1 0), 2.8 Å (−1 1 1), 2.2 Å (−2 0 2), 1.6 Å (−3 1 1). From the observation of weak diffraction spot/ring patterns of AgO along with strong Ag SAED pattern, we concluded that the possible core–shell nature of Ag NPs. The crystallographic phases of Ag NPs were polycrystalline in nature for all the four cases and no differences was observed.

The SPR peaks of NPs colloidal solution is presented in inset of Figs. 4(b), (d) and 5(b), (d) for NP-5, NP-15, NP-30 and NP-45, respectively. The inset figures depict SPR peak position at ~417 nm, ~414 nm, and ~411 nm, ~413 nm with a broad plasmon band for NP-5, NP-15, NP-30 and NP-45, respectively. Extension of the peak edge toward visible wavelength could have resulted in light gray coloration of NPs colloidal solution. Peak positions in the absorption spectra did not alter even after several weeks confirming the stability of Ag NPs [46]. Since the average size of the particles in NP-5 was large (fusing due to thermal effects), higher ordered plasmonic modes like quadruple, octopole, etc. could be significant along with dipole oscillations. Consequently, it resulted in elevation of SPR peak (with less absorbance) at longer wavelength i.e. 417 nm. Compared to this NP-15, NP-30 resulted in fabrication of smaller sized Ag NPs leading to blue shift of the SPR peak (413 and 411 nm). In NP-45, SPR bandwidth was larger since it might contain Ag NPs of larger dimensions along with small dimensioned particles. Probably, this could be the reason for observed small hump in the absorption spectra. Furthermore, the extension of shoulder in absorption spectra could be from partial agglomeration. As per the spectra, absorbance in NP-30 was strong enough to reveal higher density of Ag NPs compared to NP-5, NP-15 and NP-45. Higher magnification TEM bright field images of NP-5 revealed the presence of core shell type Ag NPs [Fig. 6(a)], Ag nanocubes [Fig. 6(b)]. Magnified image of core–shell type Ag NPs is shown in Fig. 2 of SI with a shell thickness of ~4 nm.

NLO studies of the prepared Ag suspensions were carried out using fs DFWM (BOXCAR-geometry) technique with ~40 fs pulses at 800 nm. Third order susceptibility of the Ag colloids was estimated from the recorded DFWM transient. Compared to the well known method of NLO characterization Z-Scan, DFWM provides temporal information like dephasing time of the surface plasmon oscillations in Ag NPs along with third order processes Fig. 7(a)–(d)illustrate the fs-DFWM transients of the (a) NP-5,

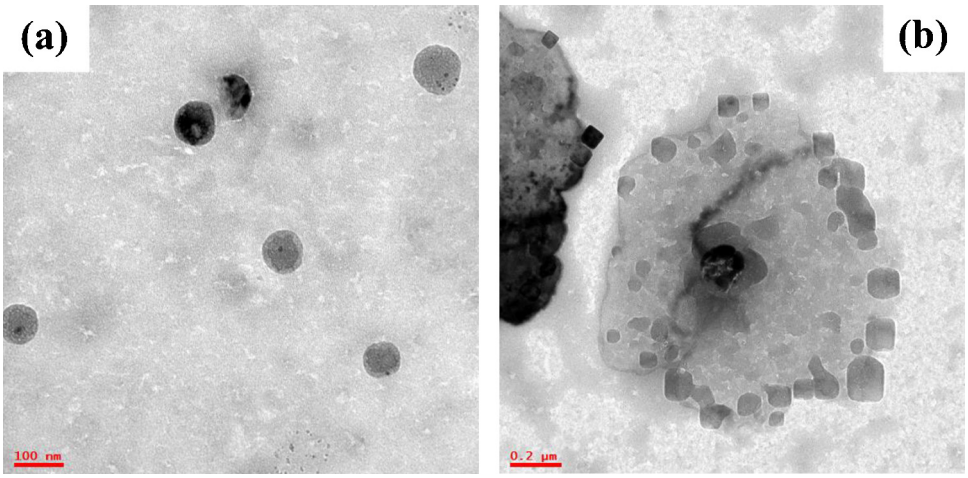

Fig. 6. TEM images of (a) core–shell type Ag nanoparticles obtained, (b) Ag colloids in NP-5 displaying cubic morphology.

(b) NP-15, (c) NP-30 and (d) NP-45, respectively. Before recording the fs-DFWM transient of Ag suspensions DFWM signal was obtained with critically phase matched Type II BBO and was optimized through the alignment of three fundamental beams and proper rotation of the crystal. Transients were recorded for each Ag suspension after slight mechanical movement of the cuvette to avoid damage to sample and to get rid of any possible aggregation at the time of data recording. Fast photodiode (SM1PD2A) was used to record the DFWM transients without subjecting it to saturation. Along with Ag suspensions in double distilled water, DFWM transient of a reference sample carbon tetrachloride was recorded at similar experimental conditions. CCl_4 is a suitable reference in fs regime since it will not depict the molecular orientational nonlinearity [74]. DFWM transients are sensitive to both electronic and vibrational signatures. As shown in Fig. 7(a)–(d) the coherent spikes in each transient at zero delay can be elucidated as the probe beam being diffracted from optical grating formed by interaction of incoming electric fields [75]. Time zero at which normalized voltage is maximum is expected to be from the electronic susceptibility [76]. The arm of transient depends on solvent-colloid interactions. Intensity dependent cubic nonlinearities of Ag suspensions were confirmed from the data obtained with input laser intensity versus DFWM signal power in logarithmic scales. Slope of the plot retrieved was ~3 from the data presented in Fig. 8 and evidently indicating the observed nonlinearity was purely cubic in nature. The intensity of DFWM [77,78] beam being is given by

$$I_{\mathrm{DFWM}} = \mathrm{const.}\frac{|\chi^{(3)}|^2}{n^4}L^2I^3 \quad (1)$$

Possible nonlinear absorption mechanisms in Ag colloids in water were discussed in our earlier Z-scan experiments where we could not decouple the third order and fifth order processes [46]. In the

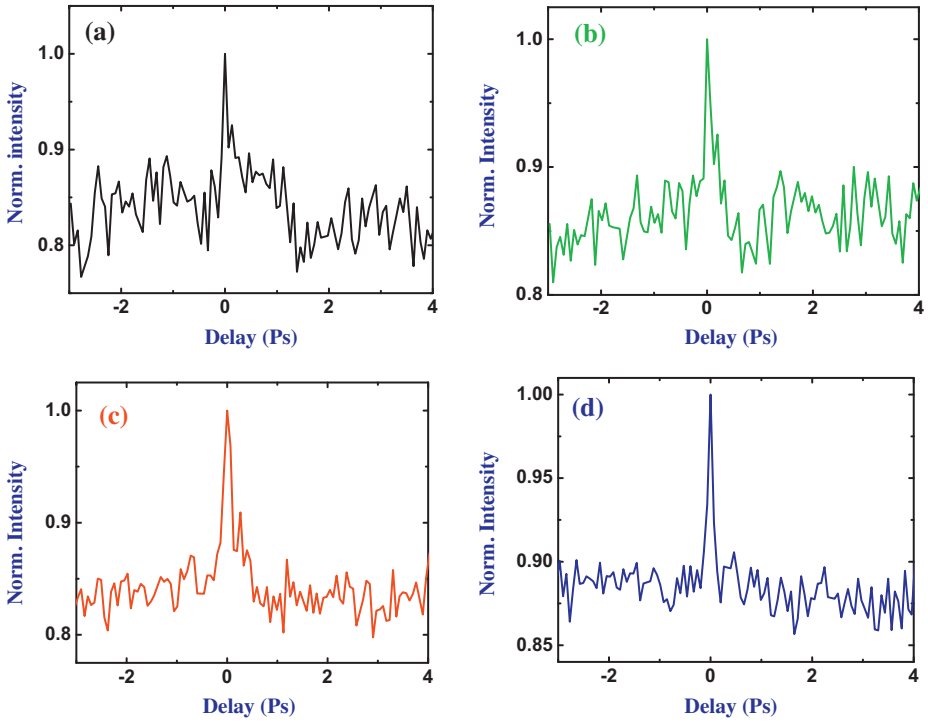

Fig. 7. DFWM transients of the Ag colloids (a) NP-5 (b) NP-15 (c) NP-30 and (d) NP-45 recorded with laser pulses of duration ~40 fs at a wavelength 800 nm. Input peak intensity used was ~10^{11} W/cm^2.

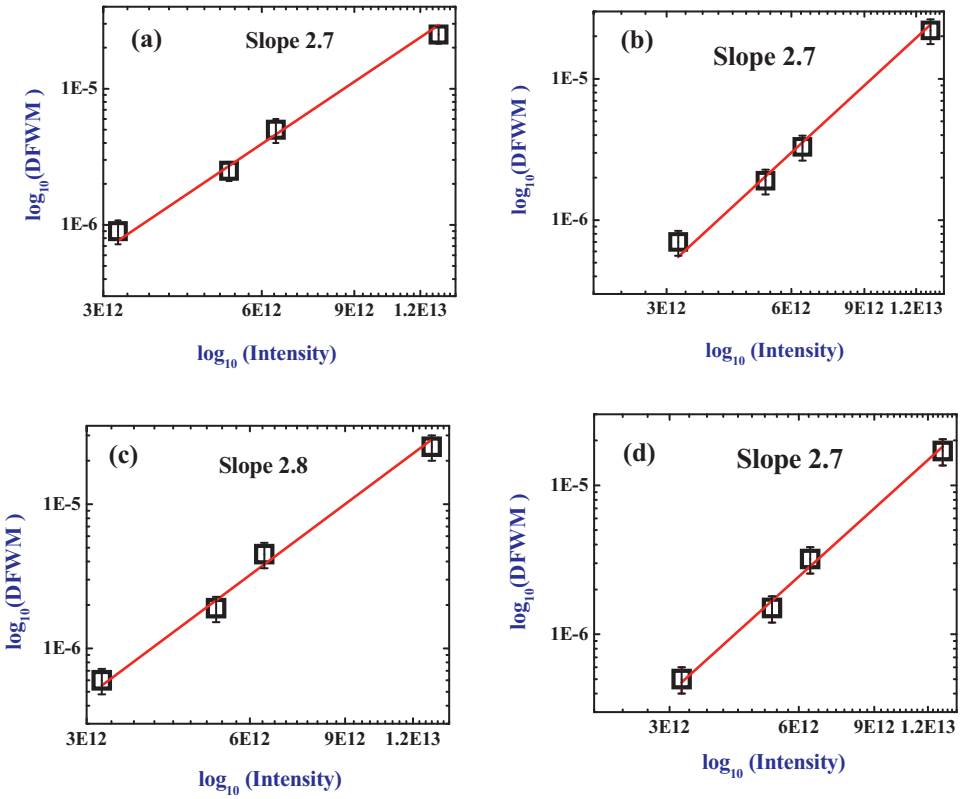

Fig. 8. Input intensity versus DFWM signal on a logarithmic scale for (a) NP-5, (b) NP-15, (c) NP-30 and (d) NP-45. Error bar was estimated to ±20%.

present case of DFWM, we provide the confirmation of a pure third order process. DFWM trace was recorded for different input pulse energies of ~45, ~22, ~18, and ~11 μJ. The effective third order nonlinearities of the Ag suspensions in double distilled water were estimated through equation [79] by comparing DFWM signals of a reference sample (CCl_4) measured under same experimental conditions.

$$\chi_S^{(3)} = \sqrt{\frac{I_S}{I_R}}\left(\frac{n_S}{n_R}\right)^2\left(\frac{L_R}{L_S}\right)\left(\frac{\alpha L}{e^{\frac{-\alpha L}{2}}(1-e^{-\alpha L})}\right)\chi_R^{(3)} \quad (2)$$

where I is the DFWM signal intensity, n is the linear refractive index, L is the sample length and α is the linear absorption coefficient of the colloidal double distilled water at 800 nm. Subscripts S, R represents the sample and reference, respectively. Estimated $\chi^{(3)}$ could have contributions from water as well as Ag NPs. Estimated linear transmittance (LT) for NP-5, NP-15, NP-30 and NP-45 were ~0.96, ~0.98, ~0.92 and ~0.94 respectively. $\chi^{(3)}$ of Ag colloids in distilled water was estimated from Eq. (2) by considering carbon tetrachloride ($n_0 - 1.45$) as reference solution whose $\chi^{(3)}$ in fs regime was approximated as $\sim 4.4 \times 10^{-14}$ e.s.u. Estimated $\chi^{(3)}$ of colloidal solutions were $\sim 1.2 \times 10^{-14}$ e.s.u., $\sim 1.3 \times 10^{-14}$ e.s.u., $\sim 1.1 \times 10^{-13}$ e.s.u., $\sim 1.8 \times 10^{-14}$ e.s.u. for NP-5, NP-15, NP-30 and NP-45, respectively. The above mentioned values had contributions from Ag NPs and double distilled water. To obtain pure contribution of Ag NPs, $\chi^{(3)}$ of double distilled was estimated and found to be $\sim 1.3 \times 10^{-16}$ e.s.u. By subtracting the contribution of pure distilled water we could get exclusive contribution of Ag NPs to $\chi^{(3)}$.

$$\chi_{\text{total}}^{(3)} = \chi_{\text{Ag}}^{(3)} + \chi_{\text{water}}^{(3)} \quad (3)$$

Estimated $\chi^{(3)}$ of pure Ag NPs were 1.18×10^{-14} e.s.u., 1.27×10^{-14} e.s.u., 1.09×10^{-13} e.s.u., 1.78×10^{-14} e.s.u., for AgNP-5, AgNP-15, AgNP-30 and AgNP-45, respectively. The main reason for observed nonlinearity in Ag colloids is excitation of LSPRs in Ag NPs such that absorption prevails at the site of NPs. These LSPR might lead to nonlinear absorption of the incident photons. Recently, Li et al. [80] reported ultrafast third order optical nonlinearities of Au nanoprisms (average edge length of ~170 nm) prepared by chemical methods and recorded a $\chi^{(3)}$ of $\sim 10^{-14}$ e.s.u. They examined the ultrafast time response (~482 fs) of sample using the technique of Optical Kerr effect. From our data presented in Fig. 7 it is apparent the involved relaxation processes were ultrafast, with lifetimes <2 ps. Further detailed studies are necessary to exactly decouple the dephasing and population relaxation times from these transients and will be a subject of our future studies.

To investigate role of incident angle on the outcome of ablation, absorbance, SPR peak position, average size of NPs, DFWM signal intensity of NPs were plotted against the angle of incidence. Fig. 9(a) illustrates effect of angle of incidence on the absorbance of fabricated Ag suspensions in water. We observed the yield of Ag nanoparticles in case of NP-30 was greater than in cases of NP-5, NP-15 and NP-45. Fig. 9(b) depicts the SPR peak position of colloidal solutions as a function of incident angle. Minimum SPR peak position (411 nm) was observed for NP-30. If SPR peak wavelength shifts toward blue spectral region then the average sizes NPs are expected to be smaller. Second observation confirmed from the data presented in Fig. 9(c) was that average size of the NPs in NP-30 was ~14 nm. Fig. 9(c) data clearly suggests minimum average size was obtained for NP-30 compared to others. Fig. 9(d) illustrates the strength of DFWM signal intensities of NP-5, NP-15, NP-30 and NP-45. This data also suggested that DFWM signal intensity was higher in the case of NP-30. Furthermore, estimated $\chi^{(3)}$ was also found to be higher for NP-30. The error bars (5%) in Y-axes are introduced in the plots 9(a), 9(c) and 9(d) where as in 9(b) the error was ±0.25%. Similarly, X-axis error bars for Fig. 9 was ~5%.

To investigate the precise effect of angle of incidence on ablation products, required energy per pulse was estimated in each case by

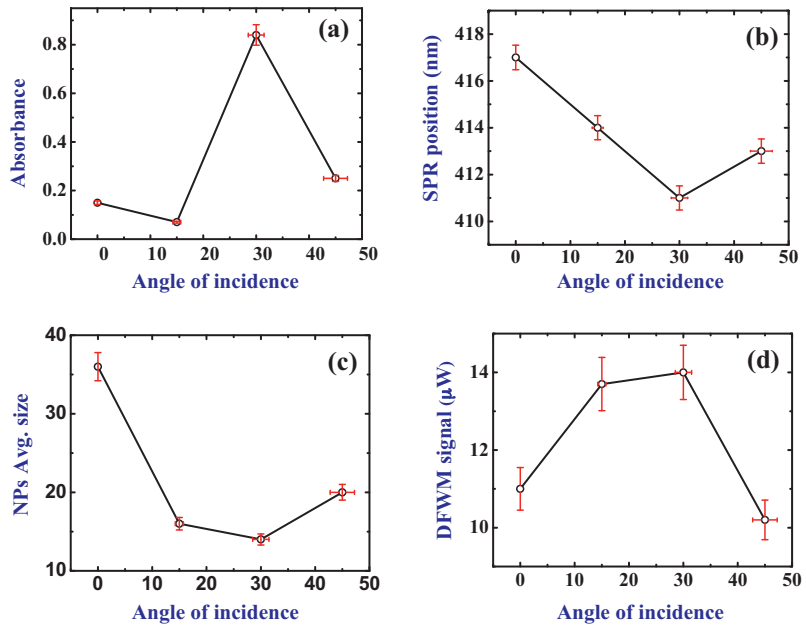

Fig. 9. (a) Absorbance (b) SPR peak position (c) Average size of Ag nanoparticles and (d) DFWM signal intensity of Ag colloids NP-5, NP-15, NP-30 and NP-45 plotted against the angle of laser incidence. Error bars in *X* and *Y* axes indicate the errors in measurements of corresponding quantities. Solid lines are a guide to eye.

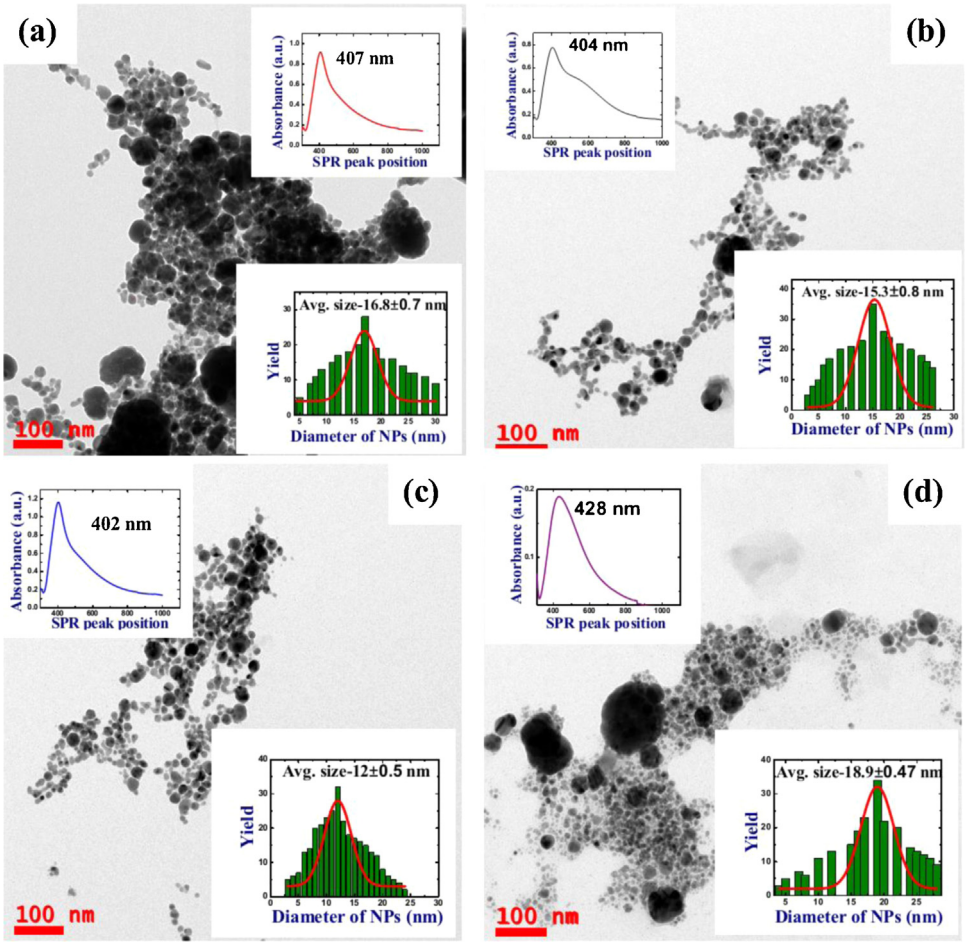

Fig. 10. TEM images of the Ag nanoparticles [prepared at constant fluence by adapting the pulse energy with respect to the estimated beam waist] of the Ag colloids (a) NP-5, (b) NP-15, (c) NP-30 and (d) NP-45. Insets show the variation of average size of NPs and the absorption spectra. Solid lines are only a guide to eye.

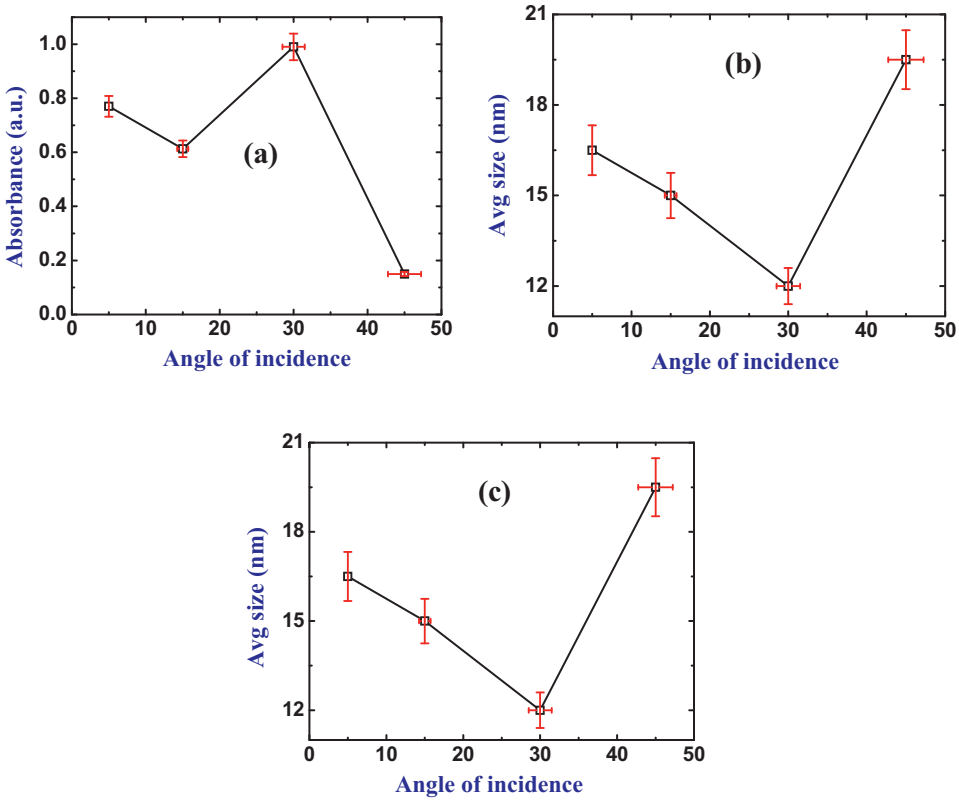

Fig. 11. (a) Absorbance, (b) SPR peak position, (c) Average size of the Ag nanoparticles [prepared at constant fluence by adapting the pulse energy with respect to the estimated beam waist] NP-5, NP-15, NP-30 and NP-45 plotted against the angle of laser incidence. Error bars in *X* and *Y* axes indicate the errors in measurements of corresponding quantities. Solid lines are a guide to eye.

considering the area of crater in an attempt to maintain constant fluence on target surface. Those energies were ~200 μJ, ~280 μJ, ~356 μJ, and ~422 μJ, for the angles of incidence 5°, 15°, 30°, and 45°, respectively to maintain a constant fluence of ~4.2 J/cm^2 on the target surface. Fig. 10(a)–(d) depicts the TEM images of Ag nanoparticles prepared at constant fluence by adapting the pulse energy with respect to the estimated beam waist. In these set of experiments the average particle size in 5° case was observed to be higher compared to earlier experiments. This could possibly be due to (a) errors in the measurement of angle (very close to normal incidence) (b) TEM images recorded at different days/times after the exposure to laser pulses due to non-availability of the instrument (c) targets from different batches being used. Further investigations are pending to identify this discrepancy. Fig. 11(a)–(c) shows the behavior of SPR peak, absorbance and average size of NPs produced versus the incident angle used for ablation. Error bars with ~5% of error in *Y*-axes were introduced in the plots 11(a), 11(c) where as in 11(b) error was ~1%. Similarly *X*-axis error for three plots in Fig. 11 was ~5%. The error bars represent errors in measurements of angles, average sizes, SPR peaks, etc. obtained in each experiment carried out more than once. The overall dependence of SPR peak position, absorbance, and average size of NPs generated did not vary greatly compared to the earlier set of experiments. From these observations we could conclude that in addition to the fluence of laser, angle of incidence also plays a significant role in ablation to some extent. Other details of this study are presented in Fig. 7 of SI.

Recently Al-Mamum et al. [81] investigated the formation of Al_2O_3 NPs using ns ablation of Al target in distilled water. The effects of target inclination (different angles of laser incidence) and pH were investigated and they observed that NPs size decreased with increasing angle. In our case too we observed that NPs size decreased until 30° incidence angle while the trend reversed for NPs generated at an angle of 45°. Observed differences in NPs fabrication can be possibly be explained in four ways (a) anisotropic intensity distribution at focus (b) fluence variation at the focus at different angles (c) surface plasmon resonance angle of silver and (d) cavitation bubble oscillations.

Firstly, intensity profile of Gaussian beam at the focus is approximated to anisotropic Gaussian function mentioned as following

$$I(x,y,z) = I_0 e^{\left\{\frac{-2(x^2+y^2)}{r_0^2} - \frac{2z^2}{z_0^2}\right\}} \quad (4)$$

where I_0 is the incident beam intensity, r_0 is the waist across lateral intensity profile and z_0 is the waist across axial intensity profile. For a focused laser beam intensity distribution has two FWHMs corresponding to two intensity profiles, i.e. one is perpendicular to direction of propagation denoted by FWHM$_r$ [lateral] and other one is FWHM$_z$ [axial] along the direction of propagation (*Z*-axis) as depicted in Fig. 12. These intensity FWHMs of focused laser beam are related to beam waist (ω_0) in [82]

$$\mathrm{FWHM}_r = 2\omega_0\sqrt{\left(-\frac{1}{2}\ln\frac{1}{2}\right)} \quad (5)$$

$$\mathrm{FWHM}_z = 2\pi\omega_0^2 \quad (6)$$

When the laser beam is focused on target at zero angle of incidence, lateral intensity distribution only causes the ablation. If the angle of incidence is increased, slant incidence of laser beam on the target surface will be affected by both lateral and axial intensity distributions of laser beam. This effect could be stronger when ablation takes place at an angle of 30°. Consequently, laser impact might provide a large metallic melt reservoir to fabricate large number of NPs. In addition, axial intensity distribution could work as second source for manipulating the metallic melt generated through

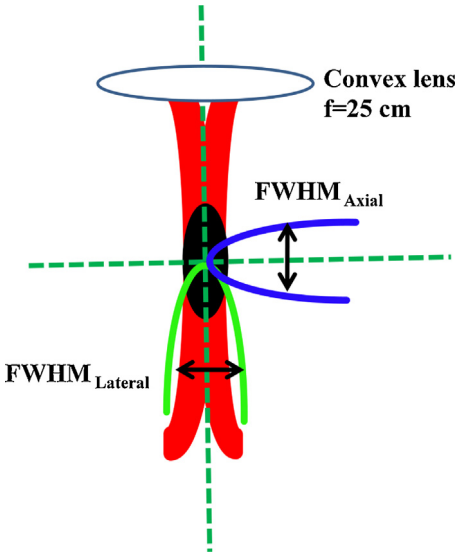

Fig. 12. Anisotropic intensity distribution of the laser beam at the focus and its lateral and axial beam waists.

lateral intensity profile resulting in fabrication of NPs with smaller sizes. For angles of incidence <30°, lateral intensity could only have played a role in determination of size of metallic melt and ablation mechanism. In the case of 45°, it is expected that some part of laser beam at focus might be reflected from target surface even though lateral and axial intensities were involved in ablation process. Consequently, we believe that ablation at this angle could not provide a better yield.

Secondly, as per data presented in Fig. 9 differences in the yield of NPs, SPR peak positions, average size of NPs are not solely from fluence variation. If the fluence decreases with increasing angle, fabrication of Ag NPs and then correspondingly, yield should decrease from 5° to 45°. But our observation (higher yield was observed at 30°) was in contrary to previous reports describing the increase of yield as the function of fluence. Higher yield of NP-30 was confirmed from the UV–vis absorption spectra. This clearly suggests that some other parameter played a significant role in determination of yield and the size of NPs.

Thirdly, the parameter that could affect outcome of ablation is SPR angle of Ag target surface. It is well established that SPR angle for Ag surface lies in the range of 30°–40° illustrating that efficient coupling of the incident laser beam with the surface plasmons on the Ag target surface occurs at 30° [83]. This leads to absorption of laser pulse energy to a large extent compared to the other three cases and hence the higher rate of ablation resulting in observation of a higher yield. Yield at 45° angle of incidence was lower compared to 30° angle of incidence could be from partial absorption of the laser pulse energy by target surface (which is due to partial reflection). Nath et al. [84] explained the observation of smaller sized TiO_2 NPs when the target was placed above and below focal plane was because of collisional frequency which depends on the plasma temperature and thus input laser fluence. As a consequence, smaller sized Ag NPs were observed when the ablation was carried out at large nonzero angles compared to zero angle of incidence. This is in agreement with the argument that larger sized particles were observed for 5°, which provided higher collisional frequency leading to coalescence. However, as mentioned above Al-Mamum [81] only dealt with the generation of Al NPs (with ns pulses) at oblique incidence of laser, but in the present experiments we tried to investigate the characteristics of fabricated NSs also through SERS technique along with NPs.

Fourth argument could be the formation of cavitation bubbles of different sizes corresponding to four angles of incidence. Depending on the dimensions of bubble, oscillations may vary. Repetition rate of the ps pulses used was 1 kHz resulting in a temporal interpulse distance of 1 ms. Since the cavitation bubbles sustain form 10^{-6} to 10^{-4} s, we do believe in dependence of the cavitation bubble radius on incident angle. However, further detailed studies are essential to confirm this. Following detailed experiments, Wagener et al. [85] explained transient interference of cavitation bubble with incoming pulses prevails only when the temporal separation between the pulses decreases i.e. in the case of lasers with high repetition rate greater than 1 kHz. However, we expect differences in the cavitation bubble formation/dynamics during ablation for different angles of incidence. Intense investigations are essential to comprehend the bubble dynamics at oblique angles of incidence.

3.2. Characterizations of Ag nanostructured substrates

Morphologies of laser exposed portions of Ag substrates were investigated through FESEM and AFM imaging techniques. Fig. 13 depicts the surface morphologies of NS-5 and NS-15. Fig. 13(a), (c) illustrate the FESEM images of laser exposed portions of Ag substrates corresponding to NS-5 and NS-15. Fig. 13(b), (d) represents the AFM images of NS-5 and NS-15, respectively. AFM images exhibited lateral nanostructures of dimensions <200 nm. Similarly, Fig. 14 depicts the surface morphologies of NS-30 and NS-45. Fig. 14(a), (c) illustrate the FESEM images of laser exposed portions of Ag substrate corresponding to NS-30 and NS-45, respectively. Fig. 14(b), (d) represents the AFM images of NS-30 and NS-45, respectively. AFM images once more confirmed presence of lateral nanostructures on the surface of NS-30. AFM image of plain silver substrate is presented in Fig. 3 of SI.

Ablation of targets was carried out in a controlled manner without changing the writing conditions except the angle of incidence. The surface topography of laser exposed portions of the substrates did not demonstrate evident major differences in their nanostructures. Raman spectra of adsorbents were recorded from nano-textured NS-5, NS-15, NS-30 and NS-45. The performance of NS-5, NS-15, NS-30 and NS-45 was investigated by recording the Raman spectra of R6G with excitation wavelengths of 785 nm and 532 nm. Fig. 15(a)–(d) depicts the Raman spectra of R6G (~10 μL drop) placed on laser exposed portion to form a monolayer of analyte (excitation wavelength of 785 nm). Large quantity of analyte (multi-layered) generally inhibits activity of nanostructures on the substrate. Furthermore, activity of substrate depends on the distance between nanostructure and analyte molecule (typically should be few nm). To compare the Raman spectra [excitation wavelength of 785 nm] of analyte from laser ablated Ag surface, the Raman spectra of R6G from plain Ag surface (blue), Si substrate (black) were also recorded and data is presented in Fig. 4 of SI. Estimated intensity enhancements of the Raman mode at 1360 cm^{-1} for 25 μM concentration R6G were ~13, ~12, ~25 and ~14 from NS-5, NS-15, NS-30 and NS-45, respectively [reference spectrum R6G of higher concentration is shown in 5 of SI]. Comparison is shown in 6 of SI. In a similar fashion, the Raman spectra of R6G of 25 nM concentration were also recorded from four substrates and compared as shown in Fig. 16. Four Ag substrates demonstrated the Raman signatures of R6G in accordance with reports in literature [86,87]. The performance of each substrate was evaluated through estimation of enhancement factor (EF) [88].

$$EF = \frac{I_{SERS}}{I_{Raman}} \frac{N_{Raman}}{N_{SERS}} \quad (7)$$

where I_{SERS} is the integrated intensity of R6G band under consideration from the nanostructured Ag substrate and I_{Raman} is the integrated intensity of the same Raman band obtained via focusing

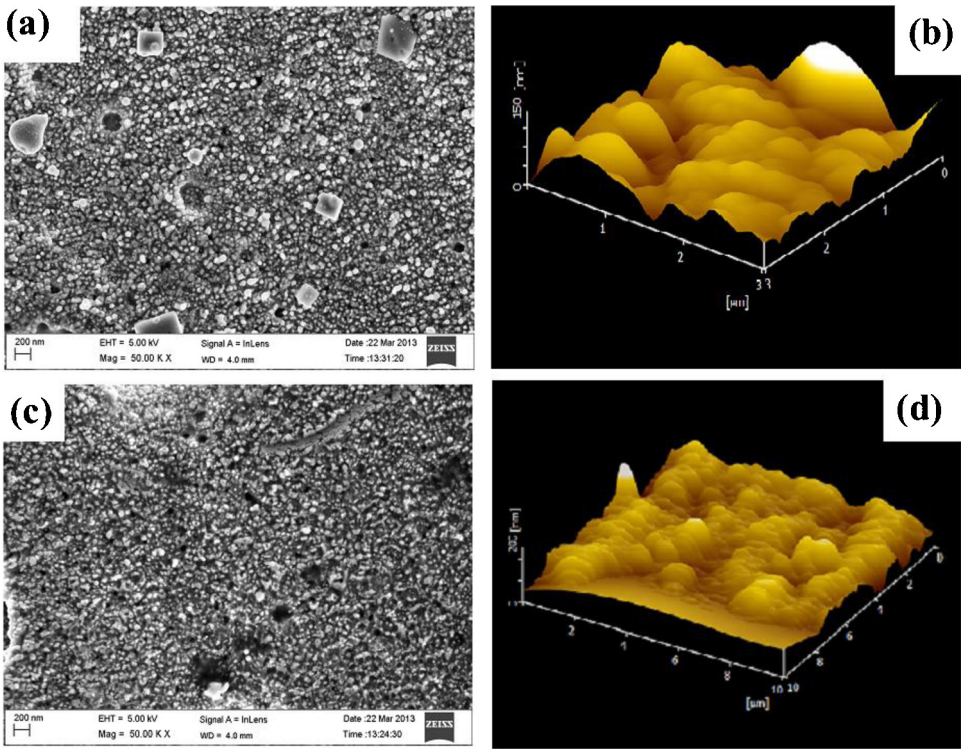

Fig. 13. (a) FESEM imaging of laser exposed Ag substrates NS-5, (b) AFM imaging of laser exposed Ag substrates NS-5, (c) FESEM imaging of laser exposed Ag substrates NS-15 and (d) AFM imaging of laser exposed Ag substrates NS-15.

the laser on R6G (0.25 M) liquid on the Silicon substrate as shown in Fig. 5(a) of supporting information. Similarly, N_{SERS} is the number of molecules constituting the first monolayer of adsorbed molecules on the nanostructured substrate surface under the laser spot area and N_{Raman} is the number of molecules in the bulk R6G solution on Si target. Following procedure reported by Su et al. [89] estimated the values of N_{SERS}, N_{Raman} were 120, 5×10^9, respectively, via considering the adsorption factor [details are provided in SI]. We arrived at

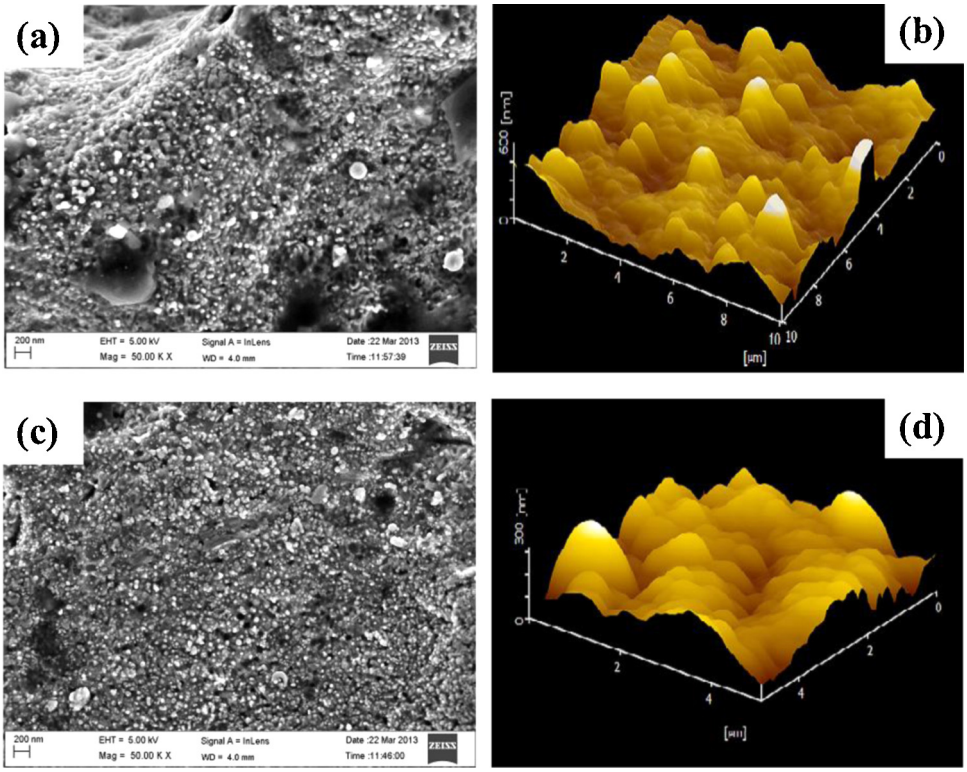

Fig. 14. (a) FESEM imaging of laser exposed Ag substrates NS-30, (b) AFM imaging of laser exposed Ag substrates NS-30, (c) FESEM imaging of laser exposed Ag substrates NS-45 and (d) AFM imaging of laser exposed Ag substrates NS-45.

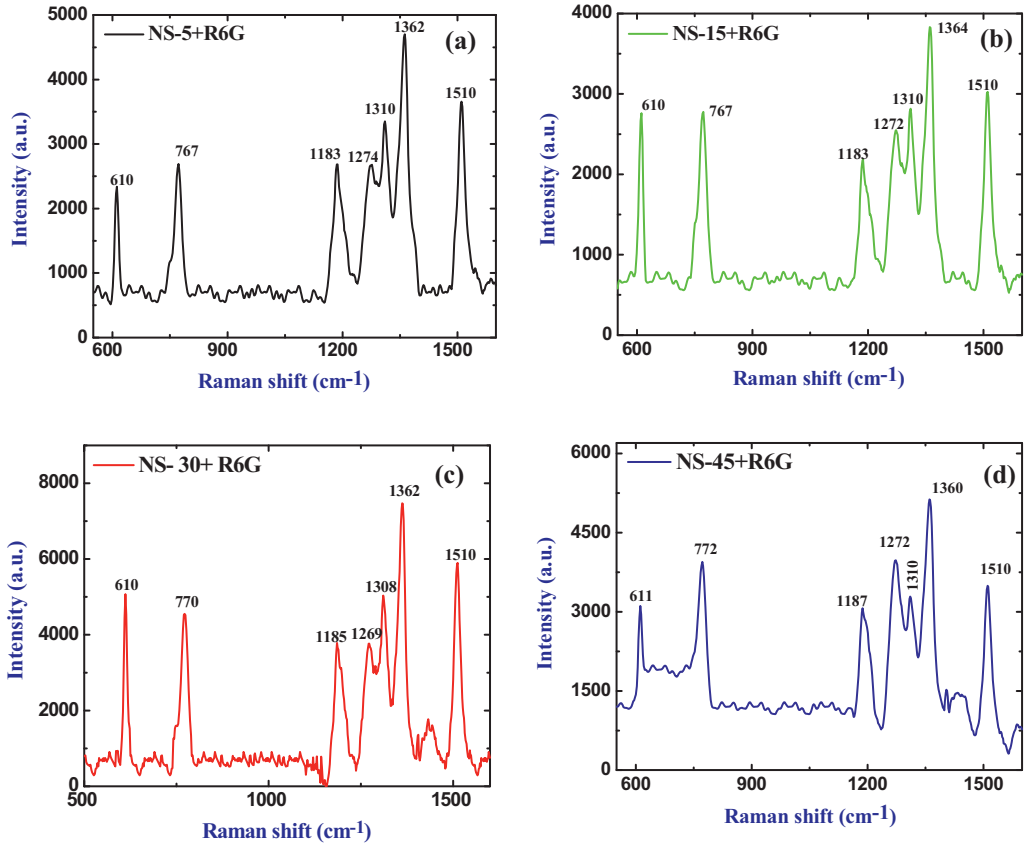

Fig. 15. Raman spectra of R6G (25 μM) recorded from the (a) NS-5, (b) NS-15, (c) NS-30 and (d) NS-45 with an excitation wavelength 785 nm. Time of integration for each spectrum was 10 s.

this estimate considering the beam waist at the focus as ~0.65 μm for 532 nm excitation, size of the R6G molecule as 2×10^{-18} m^2 [90] For aromatic C—C stretch mode corresponding to 1362 cm^{-1}, estimated enhancement factors were 2.5×10^8, $\sim 2.6 \times 10^8$, $\sim 5 \times 10^9$ and $\sim 3.4 \times 10^8$ from the substrates NS-5, NS-15, NS-30 and NS-45, respectively. Estimated intensity enhancements and enhancement factors revealed a superior performance of NS-30 (prepared at 30°) compared to others for both μM and nM concentrations of R6G excited with 785 nm, 532 nm wavelengths.

After cleaning (with acetone) and sonication, the four substrates were utilized again to record the Raman spectra of a high explosive molecule of 5 amino,3-nitro-1H-1,2,4-nitrozole (ANTA) dissolved in acetonitrile (5 mM and 5 μM concentration). The spectra are shown in Fig. 17(a), (b)for typically mM and μM concentrations, respectively. As shown in Fig. 17, some of the dominant modes observed [91] were 470 cm^{-1}, 488 cm^{-1} (both are NO_2 deformation), 724 cm^{-1} (ring deformation), 843 cm^{-1} (NO_2 deformation + Ring deformation), 1026 cm^{-1} (N1–N2–C3 bend), 1125 cm^{-1} (NN-symmetric stretch), 1340 cm^{-1} (C–NO_2 symmetric stretch), 1530 cm^{-1} (C–NH_2 asymmetric stretch + NH_2 bend), 1588 cm^{-1} (C–NH_2 symmetric. stretch + NH_2bend). Estimation of enhancement factors were carried out by comparing the Raman spectra in Figs. 16(a) and 14(b) with the Raman spectra of ANTA (0.1 M) obtained from a glass substrate [Fig. 5(b) of SI]. For C–NO_2 symmetric stretch mode corresponding to 1340 cm^{-1}, estimated values of N_{SERS}, N_{Raman} were $\sim 1.6 \times 10^9$, $\sim 4 \times 10^{11}$, and respectively. Estimated enhancement factors for the 1340 cm^{-1} mode were $\sim 4.1 \times 10^3$, $\sim 5.5 \times 10^3$, $\sim 9.7 \times 10^4$, and $\sim 4 \times 10^3$ from the substrates NS-5, NS-15, NS-30 and NS-45, respectively via considering the adsorption factor(η) as 0.6. Similarly, estimated values of N_{SERS}, N_{Raman} were $\sim 0.8 \times 10^6$, $\sim 1.6 \times 10^{11}$, and, respectively for 5 μM concentration of ANTA (C–NO_2 symmetric stretch mode corresponding to 1340 cm^{-1}). Estimated enhancement factors were $\sim 8.5 \times 10^4$, $\sim 4.2 \times 10^5$, $\sim 1.1 \times 10^6$, and $\sim 4 \times 10^5$ from the substrates NS-5, NS-15, NS-30 and NS-45, respectively via considering the adsorption factor(η) as 0.4. As per our observations and estimation of enhancement factors for R6G and ANTA (both mM and μM) NS-30 succeeded in displaying stronger enhancements (9.7×10^4, 1.1×10^6) compared to other three substrates.

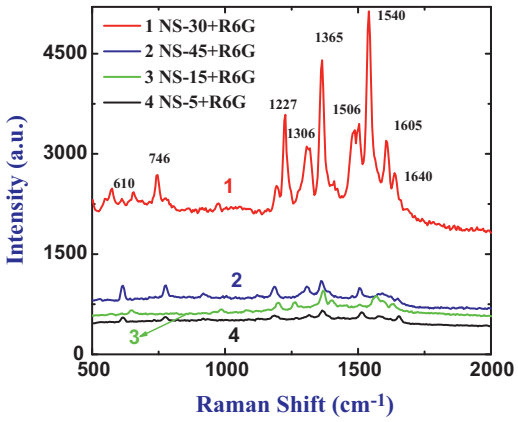

Fig. 16. Raman spectra of R6G (25 nM) recorded from the NS-5, NS-15, NS-30, and NS-45 with an excitation wavelength 532 nm and an integration time 5 s.

The most important reason behind observed enhancement of the Raman signatures is corrugated surface achieved by laser ablation acting like a random grating and supporting excitation of both localized surface plasmons (presence of Ag NPs grains) and surface plasmon polaritons (presence of random grating). Coupling of incident photon to surface plasmons of nanomaterials determines the

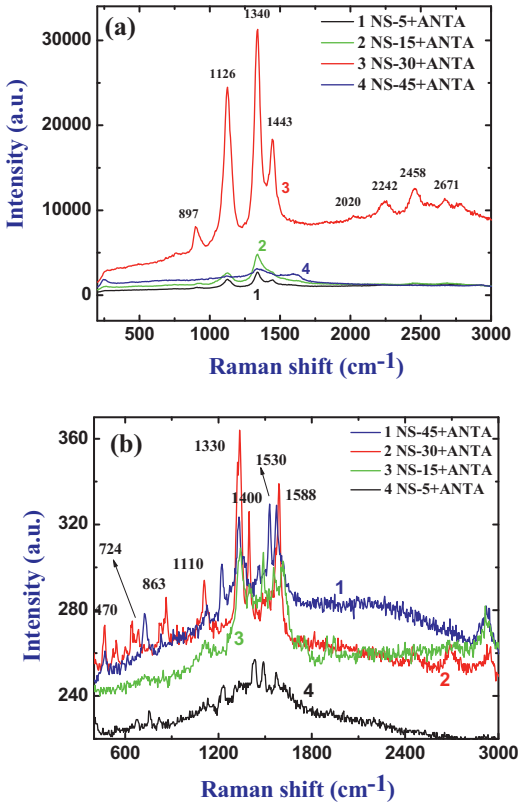

Fig. 17. Raman spectra of ANTA recorded from NS-5, NS-15, NS-30 and NS-45 with an excitation wavelength 532 nm for (a) 5 mM concentration, (b) 5 μM concentration. Time of integration for each spectrum was 5 s for data presented in (a) and 0.5 s for data presented in (b).

amount of electric field in the vicinity of nanomaterials. Essential condition for coupling in the case of surface plasmon polaritons is spacing of grating on metallic target. Similarly, size of NSs (and NPs) and wavelength of excitation are key parameters influencing the coupling of incident light to localized surface plasmons. Effective coupling of incident photon with surface Plasmons of nanomaterials enables nano-tips to act as periodically oscillating dipole antenna with an oscillation frequency of incident radiation. Consequently, an analyte molecule within the vicinity of nano-tip experiences collective electric field of incident photons and field provided by radiating dipole. Consequently, enhancement of the Raman signals from both plasmons (localized and propagating) plays a critical role.

In addition to the enhancement of Raman signatures of analytes from laser exposed portions of Ag substrates, degree of roughness and topology of surfaces (resulting from oblique laser incidence) could have played a significant role. Similar to the case of colloids, ablation of Ag at 30° incident angle ensured the surface to contain additional NSs and corrugated gratings compared to NS-5, NS-15 and NS-45. In the case of NS-30, surface plasmon polaritons could have caused effective ablation whereas LSPRs could have played a crucial role in elevating Raman signatures moderately. Thus, NS-30 was consistently providing large enhancement factors and efficient detection. Furthermore, we succeeded in utilizing the targets for identification of two different analytes separately. Significant increase in the yield of NPs production can be achieved by using different methodologies reported recently by different groups [92,93]. For example, Messina et al. [92] utilized continuously-fed wire in liquid flow for generating Ag NP's 15 times more efficiently compared to a planar target. Dell'Aglio et al. [93] successfully employed a collinear double pulse ablation technique for producing higher concentration Ag NPs. They could also correlate the SPR peak of generated NPs to the radius of cavitation bubble. Further detailed studies in this direction with fs/ps pulses could results in (a) better yield of NPs (b) better control over size and distribution of generated NPs and NSs.

4. Conclusions

In summary, influence of non-zero angle of incidence on ablation of Ag substrate immersed in double distilled water was investigated. From the experimental data we could conclude that laser ablation at an angle of 30° revealed optimum results in fabrication of NPs of smaller dimensions with better yield along with optimized structured substrates through the combined effect of axial and lateral intensity profiles of the focused laser beam. Experiment which carried out at constant laser fluence (adoption of pulse energy corresponding beam waist estimated) revealed the same kind of behavior which emphasizes the effect of incidence angle on ablation. Effect of surface plasmon resonance angle of silver surface possibly could have led to efficient coupling of incident laser photons when the incidence angle was near 30°. We believe that the oblique laser incidence is advantageous since it is free from unwanted interaction of NPs fabricated by previous laser pulses with subsequent laser pulses. Furthermore, Ag substrate fabricated at 30° demonstrated better Raman signals revealing an enhancement factor of $\sim 10^9$ from adsorbed R6G molecules with 532 nm excitation. Detection of a high explosive molecule of ANTA was carried out using SERS technique with 532 nm excitation for all the four Ag substrates. Estimated enhancement factors for ANTA (both mM and μM) were in the range of 10^3–10^6. Finally, we conclude that superior rate of Ag NPs fabrication as well as Ag NSs with better performance were achieved with ablation at 30° incident angle and thus fabricated substrates can be utilized for SERS studies of various analytes for number of times with simple cleaning methodologies.

Acknowledgments

We acknowledge the continued financial support of DRDO, India. The authors also acknowledge the assistance of Mr. Durga Prasad, Centre for Nanotechnology, University of Hyderabad.

References

[1] S.I. Dolgaev, A.A. Lyalin, A.V. Simakin, V.V. Voronov, G.A. Shafeev, Fast etching and metallization of via-holes in sapphire with the help of radiation by a copper vapor laser, Appl. Surf. Sci. 109/110 (1997) 201–205.
[2] A.V. Simakin, V.V. Voronov, N.A. Kirichenko, G.A. Shafeev, Nanoparticles produced by laser ablation of solids in liquid environment, Appl. Phys. A 79 (2004) 1127–1132.
[3] P.V. Kazakevich, A.V. Simakin, G.A. Shafeev, Formation of periodic structures upon laser ablation of metal targets in liquids, Quantum Electron. 35 (2005) 831–834.
[4] T.S. Lau, G. Levi, F. Bozon-Verduraz, A.V. Petrovskaya, A.V. Simakin, G.A. Shafeev, Generation of nanospikes via laser ablation of metals in liquid environment and their activity in surface-enhanced Raman scattering of organic molecules, Appl. Surf. Sci. 254 (2007) 1236–1239.
[5] P.V. Kazakevich, A.V. Simakin, V.V. Voronov, G.A. Shafeev, Laser induced synthesis of nanoparticles in liquids, Appl. Surf. Sci. 252 (2006) 4373–4380.
[6] E. Stratakis, V. Zorba, M. Barberoglou, C. Fotakis, G.A. Shafeev, Femtosecond laser writing of nanostructures on bulk Al via its ablation in air and liquids, Appl. Surf. Sci. 255 (2009) 5346–5350.
[7] E. Stratakis, M. Barberoglou, C. Fotakis, G. Viau, C. Garcia, G.A. Shafeev, Generation of Al nanoparticles via ablation of bulk Al in liquids with short laser pulses, Opt. Express 17 (2009) 12650–12659.
[8] E. Stratakis, V. Zorba, M. Barberoglou, C. Fotakis, G.A. Shafeev, Laser writing of nanostructures on bulk Al via its ablation in liquids, Nanotechnology 20 (2009) 105303.
[9] B. Kumar, R.K. Thareja, Synthesis of nanoparticles in laser ablation of aluminum in liquid, J. Appl. Phys. 108 (2010) 064906.
[10] N. Barsch, J. Jacobi, S. Weiler, S. Barcikowski, Pure colloidal metal and ceramic nanoparticles from high-power picosecond laser ablation in water and acetone, Nanotechnology 20 (2009) 445603.

[11] E. Messina, E. Cavallaro, A. Cacciola, R. Saija, F. Borghese, P. Denti, B. Fazio, C. D'Andrea, P.G. Gucciardi, M.A. Lati, M. Meneghetti, G. Compagnini, V. Amendola, M. Marago, Manipulation and Raman spectroscopy with optically trapped metal nanoparticles obtained by pulsed laser ablation in liquids, J. Phys. Chem. C 115 (2011) 5115–5122.

[12] S. Venugopal Rao, G. Krishna Podagatlapalli, S. Hamad, Ultrafast Laser Ablation in Liquids for Nanomaterials and Applications, J. Nanosci. Nanotech. 14 (2014) 1364–1388.

[13] E. Boulais, R. Lachaine, A. Hatef, M. Meunier, Plasmonics for pulsed-laser cell nanosurgery: Fundamentals and applications, Journal of Photochemistry and Photobiology C: Photochemistry Reviews 17 (2013) 26–49.

[14] S.S. Makridis, E.I. Gkanas, G. Panagakos, E.S. Kikkinides, A.K. Stubos, P. Wagener, S. Barcikowski, Polymer-stable magnesium nanocomposites prepared by laser ablation for efficient hydrogen storage, Int. J. Hydrogen Energy 38 (2013) 11530–11535.

[15] G. Krishna Podagatlapalli, S. Hamad, S. Sreedhar, S.P. Tewari, S. Venugopal Rao, Fabrication and characterization of aluminum nanostructures and nanoparticles obtained using femtosecond ablation technique, Chem. Phys. Lett. 530 (2012) 93–97.

[16] J.C. Hulteen, R.P. Vanduyne, Nanosphere lithography: a materials general fabrication process for periodic particle array surfaces, J. Vac. Sci. Technol. A 13 (1995) 1553–1558.

[17] J. Liu, A.I. Maroof, L. Wieczorek, M.B. Cortie, Fabrication of hollow metal nano caps and their red shifted optical absorption spectra, Adv. Mater. 17 (2005) 1276–1281.

[18] K.B. Holt, A.J. Bard, Interaction of silver(I) ions with the respiratory chain of *Escherichia coli*: an electrochemical and scanning electrochemical microscopy study of the antimicrobial mechanism of micromolar Ag, Biochemistry 44 (2005) 13214–13223.

[19] S. Shrivastava, T. Bera, A. Roy, G. Singh, P. Ramachandra Rao, D. Dash, Characterization of enhanced antibacterial effects of novel silver nanoparticles, Nanotechnology 18 (2007) 225103.

[20] H. Xiaohua, K.J. Prashant, I.H. El-Sayed, M.A. El-Sayed, Gold nanoparticles: interesting optical properties and recent applications in cancer diagnostics and therapy, Nanomedicine 2 (5) (2007) 681–693.

[21] L. Braydich-Stolle, S. Hussain, J.J. Schlager, M. Claude-Hofmann, In vitro cytotoxicity of nanoparticles in mammalian germline stem cells, Toxicol. Sci. 88 (2005) 412–419.

[22] S. Porel, S. Singh, S.S. Harsha, T.P. Radhakrishnan, Nanoparticle-embedded polymer in situ synthesis, free-standing films with highly monodisperse silver nanoparticles and optical limiting, Chem. Mater. 17 (2005) 9–12.

[23] S. Ya-Ping, E.R. Jason, W.R. Harry, G. Radhakishan, Strong optical limiting of silver-containing nanocrystalline particles in stable suspensions, J. Phys. Chem. B 103 (1999) 77–82.

[24] M. Fleischman, P.J. Hendra, A.J. McQuillan, Raman spectra of pyridine adsorbed at a silver electrode, Chem. Phys. Lett. 26 (1974) 163–166.

[25] D.L. Jeanmaire, R.P.V. Duyne, Surface Raman spectroelectrochemistry Part 1 Hetero cyclic, aromatic, and aliphatic amines adsorbed on the anodized silver electrode, Annu. Rev. Phys. Chem. 84 (1977) 1–20.

[26] M. Moskovits, Surface-enhanced spectroscopy, Rev. Mod. Phys. 57 (1985) 783–826.

[27] A. Crookell, M. Fleischmann, M. Hanniet, P.J. Hendra, Surface-enhanced Fourier transform Raman spectroscopy in the near infrared, Chem. Phys. Lett. 149 (1988) 123–127.

[28] D.B. Chase, B.A. Parkinson, Surface-enhanced Raman spectroscopy in the near-infrared, Appl. Spectrosc. 42 (1988) 1186–1187.

[29] S.M. Angel, L.F. Katz, D.D. Archibald, D.E. Hongis, Near-infrared surface-enhanced Raman spectroscopy. Part II: Copper and gold colloids, Appl. Spectrosc. 43 (1989) 367–372.

[30] K. Kniepp, Surface enhanced Raman scattering and related effects, Exp. Tech. Phys. 38 (1990) 3–28.

[31] M.L. Hae, M.J. Seung, M.K. Hyung, D.S. Young, Single-molecule surface-enhanced Raman spectroscopy: a perspective on the current status, Phys. Chem. Chem. Phys. 15 (2013) 5276–5287.

[32] D. Batani, Short-pulse laser ablation of materials at high intensities: influence of plasma effects, Laser Part. Beams 28 (2010) 235–244.

[33] S. Eliezer, N. Eliaz, E. Grossman, Synthesis of nanoparticles with femtosecond laser pulses, Phys. Rev. B 69 (2004) 144119.

[34] J.K. Chen, J.E. Beraun, Numerical study of ultrashort laser pulse interactions with metal film, Numer. Heat Transf. A 40 (2001) 1–20.

[35] D.G. Shchukin, H. Mohwald, Sono-chemical nanosynthesis at the engineered interface of a cavitation micro bubble, Phys. Chem. Chem. Phys. 8 (2006) 3496–3506.

[36] V. Amendola, M. Meneghetti, What controls the composition and the structure of nano-materials generated by laser ablation in liquid solution? Phys. Chem. Chem. Phys. 15 (2013) 3027–3046.

[37] W.T. Nichols, T. Sasaki, N. Koshizaki, Laser ablation of a platinum target in water. I. Ablation mechanisms, J. Appl. Phys. 100 (2006) 114911.

[38] T.E. Itiana, On nanoparticle formation by laser ablation in liquids, J. Phys. Chem. C 115 (2011) 5044–5048.

[39] P. Mulvaney, Surface plasmon spectroscopy of nanosized metal particles, Langmuir 12 (1996) 788–800.

[40] Y. Yokata, K. Ueno, H. Misawa, Essential nanogap effects on surface-enhanced Raman scattering signals from closely spaced gold nanoparticles, Chem. Commun. 47 (2011) 3505–3507.

[41] K.A. Willets, R.P. Van Duyne, Localized surface plasmon resonance spectroscopy and sensing, Annu. Rev. Phys. Chem. 58 (2007) 267–297.

[42] X. Cui, K. Tawa, H. Hori, J. Nishi, Tailored plasmonic gratings for enhanced fluorescence detection and microscopic imaging, Adv. Funct. Mater. 20 (2010) 546–553.

[43] J. Chandezon, M.T. Dupuis, G. Cornet, D. Mystre, Multicoated gratings: a differential formalism applicable in the entire optical region, J. Opt. Soc. Am. 72 (1982) 839–846.

[44] V. Amendola, M. Meneghetti, Laser ablation synthesis in solution and size manipulation of noble metal nanoparticles, Phys. Chem. Chem. Phys. 11 (2009) 3805–3821.

[45] D. Riabininan, M. Chaker, J. Margot, Dependence of gold nanoparticle production on pulse duration by laser ablation in liquid media, Nanotechnology 23 (2012) 135603 (4 pp.).

[46] G. Krishna Podagatlapalli, S. Hamad, S.P. Tewari, S. Sreedhar, S. Venugopal Rao, Silver nano-entities through ultrafast double ablation in aqueous media for surface enhanced Raman scattering and photonics applications, J. Appl. Phys. 113 (2013) 073106.

[47] J.B. Nielsen, J.M. Savolainen, M.S. Christensen, P. Balling, Ultra-short pulse laser ablation of metals: threshold fluence, incubation coefficient and ablation rates, Appl. Phys. A 101 (2010) 97–101.

[48] F. Liang, R. Vallee, D. Gingras, S.L. Chin, Role of ablation and incubation processes on surface nano grating formation, Opt. Mater. Exp. 1 (2011) 1244–1250.

[49] J.-P. Sylvestre, A.V. Kabashin, E. Sacher, M. Meunier, Femtosecond laser ablation of gold in water: influence of the laser-produced plasma on the nanoparticle size distribution, Appl. Phys. A. 80 (2005) 753–758.

[50] Y. Liao, J.-Y. Degorce, Meunier, Laser induced formation of periodic nanostructures in silicon covered by SiO_2, Appl. Phys. A. 82 (2006) 679–682.

[51] S. Besner, A.V. Kabashin, M. Meunier, Two-step femtosecond laser ablation-based method for the synthesis of stable and ultra-pure gold nanoparticles in water, Appl. Phys. A. 88 (2007) 269–272.

[52] S. Besner, A.V. Kabashin, E.M. Winnik, M. Meunier, Ultrafast laser based green synthesis of non-toxic nanoparticles in aqueous solutions, Appl. Phys. A. 93 (2008) 955–959.

[53] S. Besner, M. Meunier, Femtosecond laser synthesis of Au–Ag nanoalloys photo induced oxidation and ions release, J. Phys. Chem. C 114 (2010) 10403–10409.

[54] N.G. Semaltianos, Nanoparticles by laser ablation, Crit. Rev. Solid State Mater. Sci. 35 (2010) 105–124.

[55] Z. Yan, D.B. Chrisey, Pulsed laser ablation in liquid for micro-/nanostructure generation, J. Photochem. Photobiol. C: Photochem. Rev. 13 (2012) 204–223.

[56] H. Zeng, X. Du, S.C. Singh, S.A. Kulinich, S. Yang, J. He, W. Cai, Nanomaterials via laser ablation/irradiation in liquid: a review, Adv. Funct. Mater. 22 (2012) 1333–1353.

[57] R.A. Ganeev, T.Q. Jia, Nano structuring of semiconductor surfaces under the action of femtosecond pulses, Opt. Spectrosc. 105 (2008) 141–146.

[58] D.B. Singh, V.K. Tripathi, Laser beat wave excitation of surface plasma wave and material ablation, Phys. Plasmas 14 (2007) 103115–103118.

[59] D.S. George, A. Onischenko, A.S. Holmes, On the angular dependence of focused laser ablation by nanosecond pulses in solgel and polymer materials, Appl. Phys. Lett. 84 (2004) 1680–1682.

[60] S. Hamad, G. Krishna Podagatlapalli, S. Venugopal Rao, Influence of picosecond multiple/single line ablation on copper nanoparticles fabricated for surface enhanced Raman spectroscopy and photonics application, J. Phys D: Appl. Phys. 46 (2013) 485501.

[61] J. Nedderson, G. Chumanov, T.M. Cotton, Laser ablation of metals: a new method for preparing SERS active colloids, Appl. Spectrosc. 47 (1993) 1959–1964.

[62] M. Prochazka, J. Stephanek, B. Vicova, J. Stephanek, B. Vlckova, P.Y. Turpin, Probing applications of laser-ablated Ag colloids in SERS spectroscopy: improvement of ablation procedure and SERS spectral testing, Anal. Chem. 69 (1997) 5103–5108.

[63] A.M. Manjon, P. Wagener, S. Barcikowski, Transfer-matrix method for efficient ablation by pulsed laser ablation and nanoparticle generation in liquids, J. Phys. Chem. C 115 (2011) 5108–5114.

[64] S. Barcikowski, A. Menéndez-Manjón, B. Chichkov, M. Brikas, R. Gediminas, Generation of nanoparticle colloids by picosecond and femtosecond laser ablations in liquid flow, Appl. Phys. Lett. 91 (2007) 083113–83123.

[65] S. Petersen, J. Jacobi, S. Barcikowski, In situ bioconjugation – novel laser based approach to pure nanoparticle-conjugates, Appl. Surf. Sci. 255 (2009) 5435–5438.

[66] S. Mukamel, Nonlinear Optical Spectroscopy, vol. 561, Oxford University Press, New York, 1995.

[67] T. Hofer, P. Cruck, W. Kaiser, Dynamics of photochemical reactions studied by degenerate four wave mixing, Chem. Phys. Lett. 224 (1994) 411–416.

[68] V. Namboodiri, M. Namboodiri, G. Flachenecker, A. Materny, Two-photon resonances in femtosecond time-resolved four-wave mixing spectroscopy – β-carotene, J. Chem. Phys. 133 (2010) 054503–54506.

[69] H. Skendarovic, Four-wave mixing with femtosecond pulses, Phys. Scr. T135 (2009) 014037 (3 pp.).

[70] G. Boudebs, K. Fedus, C. Cassagne, H. Leblond, Degenerate multiwave mixing using Z-scan technique, Appl. Phys. Lett. 93 (2008) 021118–21122.

[71] P. Wagener, S. Ibrahimkutty, A. Menzel, A. Plech, S. Barcikowski, Dynamics of silver nanoparticle formation and agglomeration inside the cavitation bubble after pulsed laser ablation in liquid, Phys. Chem. Chem. Phys. 15 (2013) 3068–3074.

[72] E.R. Jette, F. Foote, Precision determination of lattice constants, J. Chem. Phys. 3 (1935) 605–616.

[73] M. Jansen, P. Fischer, Eine neue Darstellungsmethode für monoklines Silber (I,III)-oxid (AgO). Einkristallzüchtung und Röntgenstrukturanalyse, J. Less-Common Met. 137 (1988) 123–131.
[74] K. Kamada, M. Ueda, T. Sakaguchi, K. Ohta, T. Fukumi, Femtosecond optical Kerr study of heavy atom effects on the third-order optical nonlinearity of thiophene homologues: purely electronic contribution, Chem. Phys. Lett. 263 (1996) 215–222 [Errata: Femtosecond optical Kerr study of heavy atom effects on the third-order optical nonlinearity of thiophene homologues: purely electronic contribution, 267 (1997) 402].
[75] M. Motzkus, S. Pedersen, A.H. Zewail, Femtosecond real-time probing of reactions. 19. Nonlinear (DFWM) techniques for probing transition states of uni- and bimolecular reactions, J. Phys. Chem. 100 (1996) 5620–5633.
[76] E.J. Brown, Q. Zhang, M. Dantus, Femtosecond transient-grating techniques: population and coherence dynamics involving ground and excited states, J. Chem. Phys. 110 (1999) 5772–5788.
[77] G.M. Carter, Excited-state dynamics and temporally resolved nonresonant nonlinear-optical processes in polydiacetylenes, J. Opt. Soc. Am. B 4 (1987) 1018–1024.
[78] X.F. Cao, J.P. Jiang, D.P. Bloch, R.W. Hellwarth, L.P. Yu, L. Dalton, Picosecond nonlinear optical response of three rugged poly quinoxaline based aromatic conjugated ladder polymer thin films, J. Appl. Phys. 65 (1991) 5012–5018.
[79] M. Samoc, A. Samoc, B.L. Davies, Z. Bao, L. Yu, B. Hsieh, U. Scherf, Femtosecond Z-scan and degenerate four-wave mixing measurements of real and imaginary parts of the third-order nonlinearity of soluble conjugated polymers, J. Opt. Soc. Am. B 15 (1998) 817–825.
[80] Z. Li, Y. Lu, Z. Chen, T. Liu, Z. Zhou, J. Han, J. Li, C. Jin, X. Wang, Ultrafast third-order optical nonlinearity in au triangular nanoprism with strong dipole and quadrupole plasmon resonance, J. Phys. Chem. C. 117 (2013) 20127–20132.
[81] S.A. Al-Mamum, R. Nikajima, T. Ishigaki, Tuning the size of aluminum oxide nanoparticles synthesized by laser ablation in water using physical and chemical approaches, J. Colloid Interface Sci. 392 (2013) 172–182.
[82] M. Muller, J. Squier, C.A. de Lange, J. Brakenhoff, CARS microscopy with folded BoxCARS phasematching, J. Microsc. 197 (2000) 150–158.
[83] H. Raether, Surface Plasmons on Smooth and Rough Surfaces and on Gratings, Springer-Verlag, Berlin, 1986.
[84] A. Nath, S.S. Laha, A. Khare, Effect of focusing conditions on synthesis of titanium oxide nanoparticles via laser ablation in titanium–water interface, Appl. Surf. Sci. 257 (2011) 3118–3122.
[85] P. Wagener, A. Schwenke, B.N. Chichkov, S. Barcikowski, Pulsed laser ablation of zinc in Tetrahydrofuran: bypassing the cavitation bubble, J. Phys. Chem. C 114 (2010) 7618–7625.
[86] Y. Lu, G.L. Liu, L.P. Lee, High-density silver nanoparticle film with temperature-controllable interparticle spacing for a tunable surface enhanced Raman scattering substrate, Nano Lett. 5 (2005) 5–9.
[87] L. Jenson, G.C. Schatz, Resonance Raman scattering of Rhodamine 6G as calculated using time-dependent density functional theory, J. Phys. Chem. A 110 (2006) 5973–5977.
[88] E.C. Le Ru, P.G. Etchegoin, Phenomenological local field enhancement factor distributions around electromagnetic hot spots, J. Chem. Phys. 130 (2009) 181101–181104.
[89] L. Su, W. Jia, D.P. Manzzi, L. Zhang, X. Li, Z. Gu, Y. Lei, Highly sensitive surface-enhanced Raman scattering using vertically aligned silver nano petals, RSC Adv. 2 (2012) 1439–1443.
[90] N. Tsurumachi, H. Okamoto, K. Ishii, H. Kohkami, S. Nakanishi, T. Ishii, N. Takahashi, C. Dou, P. Wen, Q. Feng, Formation of aggregates in nanohybrid material of dye molecules-titanate nanosheets, J. Photochem. Photobiol. A 243 (2012) 1–6.
[91] J.A. Ciezak, S.F. Trevino, The inelastic neutron scattering spectra of α-3-amino-5-nitro-1, 2,4 -2H-triazole: experiment and DFT calculations, Chem. Phys. Lett. 403 (2005) 329–333.
[92] G.C. Messina, P. Wagener, R. Streubei, A. De Giacomo, A. Santagata, G. Compagnini, S. Barcikowlski, Pulsed laser ablation of a continuously-fed wire in liquid flow for high-yeild production of silver nanoparticles, Phys. Chem. Chem. Phys. 15 (2013) 3093.
[93] M. Dell'Aglio, R. Gaudiuso, R. ElRashedy, O. De Pascale, G. Palazzo, A. De Giacomo, Collinear double pulse laser ablation in water for the production of silver nanoparticles, Phys. Chem. Chem. Phys. 15 (2013) 20868.